Department of Physics and Astronomy

Heidelberg University

Master thesis in Physics

submitted by

Elif Yildirim

born in Schwäbisch Hall

2024

Measurement of the ZZZ and $WW\gamma$ final states in proton-proton collisions with the ATLAS experiment

This Master thesis has been carried out by Elif Yildirim

at the

Kirchhoff-Institute for Physics

under the supervision of

Prof. Dr. Hans-Christian Schultz-Coulon

Measurement of the ZZZ and $WW\gamma$ final states in proton-proton collisions at the ATALS experiment:

The measurement of the ZZZ and $WW\gamma$ triboson states allows to probe the gauge structure of the electroweak interaction of the Standard Model and to test new physics phenomena. In this thesis, events in the purely leptonic final states are selected for both processes. The kinematic properties of the ZZZ production process are investigated in detail and the expected number of signal events is obtained for the second collision data taking campaign (Run 2) of the ATLAS detector. The first glimpse into this rare triboson state reveals very low event yields for current data taking and enables an estimation for high-luminosity operation in the future for the purely leptonic signature. For the $WW\gamma$ production process the expected number of events are estimated for the Run 3 of the ATLAS detector and the main background processes are investigated. The results in this final state are compared to an ongoing Run 2 analysis from the ATLAS Group, where deviations between both analyses are observed.

Messung der ZZZ und $WW\gamma$ Endzustände bei Proton-Proton Kollisionen am ATLAS Experiment:

Die Messung der ZZZ and $WW\gamma$ Triboson Zustände ermöglicht es, die Eichsymmetrie der elektroschwachen Wechselwirkung des Standardmodells zu prüfen und Physik außerhalb des Standardmodells zu testen. Beide Endzustände werden für den leptonische Zerfallskanal analysiert. Die kinematischen Eigenschaften der ZZZ Produktion werden detailliert untersucht und die Anzahl der zu erwarteten Ereignisse für den Run 2 des ATLAS Detektors wird bestimmt. Ein erster Einblick in diesen Triboson Zustand ergibt eine niedrige Anzahl an zu erwartenden Ereignissen für die aktuellen Daten. Diese Messung ermöglicht es jedoch, eine Abschätzung für höhere Luminositäten in der Zukunft zu tätigen. Die $WW\gamma$ Produktion wird für den Run 3 des ATLAS Detektors analysiert, wobei die Anzahl der zu erwartenden Ereignisse bestimmt und die bedeutensten Untergrundprozesse untersucht werden. Die Ergebnise dieses Endzustandes werden mit einer noch laufenden Run 2 Analyse der ATLAS Gruppe verglichen. Dabei ergeben sich abweichende Endresultate der beiden Analysen.

Contents

1 Introduction

The Standard Model of Particle Physics is the theoretical framework that describes the fundamental particles and their interactions with each other. It has been proven to be very successful in describing experimental data of particle physics phenomena. However, there are limitations in the description of the Standard Model. Some examples of open questions are the observed matter-antimatter asymmetry in the universe, the incorporation of gravity into the Model, or the phenomenon of dark matter and dark energy in the universe. The Large Hadron Collider (LHC) at CERN provides the possibility of finding answers to these questions and to further test the Standard Model. One of the precise predictions of the Model is the production of three electroweak gauge bosons. Measuring these triboson final states serves as a test of the Standard Model, whereby any deviation would be a hint to new phenomena. Therefore, studying self-interactions of electroweak gauge bosons probe physics beyond the Standard Model.

The large quantity of data recorded by the ATLAS detector during Run 2 and Run 3 allows a first glimpse into rare production processes. In this thesis, the triboson production of the ZZZ and $WW\gamma$ final states are studied with the fully leptonic decay of the heavy gauge bosons. Analysing the ZZZ and $WW\gamma$ triboson states provides the possibility to test new physics beyond the Standard Model due to the sensitivity of these final states to anomalous quartic couplings. The ZZZ production process is studied for Run 2 with an integrated luminosity of $\mathcal{L}_{int} = 140\,\text{fb}^{-1}$ and a centre-of-mass energy of $\sqrt{s} = 13\,\text{TeV}$. This final state contains three heavy Z bosons, which leads to a small cross-section. Especially in the leptonic decay channel chosen as signature, low statistics is a challenge to this analysis. The study in this thesis for Run 2 serves the purpose of providing a first glimpse into this rare triboson production process and enabling estimations for future analyses in the high-luminosity era of the LHC. The analysis of the $WW\gamma$ final states is the first study at the Run 3 centre-of-mass energy of $\sqrt{s} = 13.6\,\text{TeV}$. For comparison reasons with an ongoing Run 2 study of the ATLAS Group [1], the $WW\gamma$ process is analysed at $\mathcal{L}_{int} = 140\ \text{fb}^{-1}$.

This thesis is organised as follows: A description of the Standard Model along with the Electroweak Model is presented and the Monte-Carlo simulation process is discussed in Chapter 2. The experimental setup of the LHC machine and the ATLAS detector is explained in Chapter 3. In Chapter 4, the particle reconstruction for the ATLAS detector is described with a focus on the objects relevant to this thesis. Chapter 5 outlines the study of the ZZZ triboson state. The analysis of the $WW\gamma$ production process is detailed in Chapter 6. In Chapter 7 this thesis is concluded with a summary of the ZZZ and $WW\gamma$ studies.

Authors contribution: Performing the studies in this thesis was possible as a member of the ATLAS Collaboration. This analysis profited from the successful operation of the ATLAS experiment on the LHC and the provided frameworks and data samples by the ATLAS Group. The explicit contributions of the author are detailed in the following. The author has carried out the analysis for the ZZZ final states, whereby the MC sample used for the study is produced by the ATLAS Collaboration. For the Run 3 analysis of the $WW\gamma$ final states, all needed MC datasets are produced for this study with the support of PhD students. The author has carried out the validation of the datasets and the final study of the $WW\gamma$ process.

2 Theoretical Background

The basic building blocks of matter and their interactions are subject of the Standard Model of Particle Physics and the theoretical core of this thesis. A description of the Standard Model is presented in Section 2.1. In Section 2.2, the unified theory of the electroweak interaction is explained in more detail. Afterwards, the effect of anomalous gauge couplings are described in Section 2.3 with a model-independent extension of the Standard Model. In the last Section 2.4, the Monte-Carlo simulation process is described and the Monte-Carlo datasets are presented.

2.1 Standard Model

The Standard Model (SM) of Particle Physics is a relativistic quantum field theory based on local gauge invariance, that describes all elementary particles and their interaction via fundamental forces. The particles are arranged by their spin. Fermions carry half-integer spin of $s = \frac{1}{2}$ and bosons are spin = 1 particles. The only spin-0 particle in the SM is the Higgs boson. Fermions consist of three leptons with their corresponding neutrino and six different quarks:

$$\underbrace{\begin{pmatrix} e \\ \nu_e \end{pmatrix}, \begin{pmatrix} \mu \\ \nu_\mu \end{pmatrix}, \begin{pmatrix} \tau \\ \nu_\tau \end{pmatrix}}_{\text{Leptons}} \qquad \underbrace{\begin{pmatrix} u \\ d \end{pmatrix}, \begin{pmatrix} c \\ s \end{pmatrix}, \begin{pmatrix} t \\ b \end{pmatrix}}_{\text{Quarks}}$$

Both, leptons and quarks, carry electric charge Q measured in the unit of the elementary charge of $e = 1.602 \times 10^{-}19C$. Leptons carry $Q = \pm 1e$ and neutrinos are neutral particles with $Q = 0$. The different quark flavours are divided in up-type quarks (u, c, t) and down-type quarks (d, s, b), where up-type quarks carry $Q = +\frac{2}{3}e$ and down-type quarks $Q = -\frac{1}{3}e$. For all fermions an antiparticle state exists. These antiparticles states have exactly the same mass but carry the opposite charge [2]. The twelve fundamental particles are sorted in three generations with increasing mass scale. An overview is given in Table 2.1, where the leptons and quarks are listed according to their respective mass scale. The elementary particles interact

Table 2.1: Overview of the spin-$\frac{1}{2}$ particles, the fermions, of the SM sorted by their mass generation.

	Leptons		**Quarks**	
Mass-generation	Particle	Charge	Particle	Charge
First Generation	electron (e^-)	-1	up (u)	$-\frac{1}{3}$
	neutrino (ν_e)	0	down (d)	$+\frac{2}{3}$
Second Generation	muon (μ^-)	-1	strange (s)	$-\frac{1}{3}$
	neutrino (ν_μ)	0	charm (c)	$+\frac{2}{3}$
Third Generation	tau (τ^-)	-1	bottom(b)	$-\frac{1}{3}$
	neutrino (ν_τ)	0	top (t)	$+\frac{2}{3}$

with each other via the fundamental forces in the SM. The three fundamental forces described by the SM are the electromagnetic (EM), strong and weak force, which are mediated by exchanging a spin-1 particle, the gauge boson.

Each force is described by a quantum field theory (QFT), where the interactions are described via the exchange of spin-1 gauge fields. The SM is based on the gauge symmetry group of [3]

$$SU(3)_C \otimes SU(2)_L \otimes U(1)_Y. \tag{2.1}$$

Each of the constituent symmetry groups in Equation 2.1 correspond to a fundamental force. The group generators are associated with a gauge boson vector field, which is described in the following. An overview of each gauge boson with its corresponding mediated force is given in Table 2.2. The quantum field theory of quantum electrodynamics (QED) describes electromagnetism and is based on invariance under local phase transformations, which corresponds to an abelian $U(1)$ gauge symmetry. The force carrier is the neutrally charged and massless photon (γ). Every particle that carries electrical charge can interact electromagnetically. The quarks and gluons are the only particles in the SM that carry the so-called colour charge in addition to the electromagnetic charge. Therefore, only these particles are able to participate in the strong interaction, which is described by the field theory of quantum chromodynamics (QCD) and is mediated by eight massless gluons. These eight generators create the non-abelian symmetry group of $SU(3)$. Hence, the QCD is invariant under local $SU(3)$ phase transformations. Special properties of QCD arise due to the underlying non-abelian structure.

Table 2.2: Overview of the forces in the SM and their corresponding mediator along with the masses of the gauge bosons.

Force	Mediating Boson	Mass (GeV)
EM	Photon (γ)	0
Strong	Gluon (g)	0
Weak	W boson ($W^{\pm}$)	80.4
Weak	Z boson (Z)	91.2

The gluons can undergo self-interactions that leads to the phenomenon of colour confinement, which is the reason that only colourless bound quark states exist. These states can be composites of quark pairs referred to as mesons, or to quark triplets, denoted as baryons. This process of hadrons being produced through colour confinement is called hadronization. The weak interaction is mediated by the $W^{\pm}$ and the Z bosons. Besides the weak charge, the $W^{\pm}$ bosons also carry electrical charge of $W^{\pm} = \pm 1e$. The Z boson is electrically neutral and only carry weak charge [2]. The underlying group symmetry of the weak interaction is the $SU(2)$ symmetry and is described in more detail in the following section along with the electroweak (EW) theory, which unifies QED and the weak force.

While the SM describes the mentioned elementary interactions between the fundamental particles very accurate, the fourth fundamental force of gravity is not included. So far, gravity only plays a role on macroscopic scales and does not have an impact on sub-atomic scales. Attempts to include gravitational force into the QFT of the SM is called grand unification and is not accomplished yet [4]. The gravitational aspects in the SM are also relevant in the search for dark matter (DM), which describes non-luminous matter throughout the universe. A gravitational interacting particle that could be assign to DM is not provided by the SM so far [5]. These are examples of yet unanswered questions and establish the need for theories beyond the SM.

2.2 Electroweak Theory

The unification of the electromagnetic and the weak interaction was derived by Glashow, Salam and Weinberg in the 1960s. The combination of both forces succeeded through the $\mathrm{SU}(2)_L \otimes \mathrm{U}(1)_Y$ gauge symmetry in the GSW (Glashow, Salem, Weinberg) model [6–8]. Gauge boson masses are introduced successfully into the SM by spontaneous symmetry breaking.

The interaction of the massive gauge bosons, $W^{\pm}$ and Z, with fermions is described by the theory of the weak interaction. The weak force for leptons shows universal coupling strength for all three lepton flavours. This is not the case in the quark sector. Here, the transition between different flavours within the same generation of quarks are maximal, whereas transitions between different generations are suppressed. The neutral Z boson initiates interactions between quarks of the same flavour, whereas the transition between quark flavours is induced by the $W^{\pm}$ bosons. The transition probability of quark flavours in the weak interaction is described in terms of the unitary Cabibbo–Kobayashi–Maskawa (CKM) matrix [9,10], where the weak eigenstates (d', s', b') are related to the mass eigenstates (d, s, b) by

$$\begin{pmatrix} d' \\ s' \\ b' \end{pmatrix} = \begin{pmatrix} V_{ud} & V_{us} & V_{ub} \\ V_{cd} & V_{cs} & V_{cb} \\ V_{td} & V_{ts} & V_{tb} \end{pmatrix} \begin{pmatrix} d \\ s \\ b \end{pmatrix} . \tag{2.2}$$

The matrix elements V_{ij} are a measure for the probability of the transition between quark i and j through charged current interaction. Another special characteristic of the weak interaction is the maximal violation of parity, which was validated by the WU-experiment [11]. The parity violating nature of the weak force determines the structure of its interaction vertex. The interaction vertex must be constructed for a spin-1 boson and satisfy Lorentz-invariance, which leads to a coupling structure consisting of a vector and axial-vector (V-A). The special structure of the interaction vertex is the cause of a unique coupling property of the weak interaction, where coupling to particles differentiate between the left-handed (LH) and right-handed (RH) particle states. The weak force only couples to LH particle states and RH antiparticle states [12].

The gauge symmetry of the unified EW theory must reflect the different couplings of each force. The unification of both forces must consider this condition in the gauge symmetry. To demonstrate the construction of the electroweak symmetry group, LH fermions are grouped as doublets and their RH counterparts are defined as singlets. The first generation of fermions is used as an example with LH and RH particle states:

$$\begin{pmatrix} \nu_e \\ e^- \end{pmatrix}_L, \begin{pmatrix} u \\ d \end{pmatrix}_L \quad \text{and} \quad e_R^-, u_R, d_R \tag{2.3}$$

The symmetry group of $\mathrm{SU}(2)_L$ creates transformations of the doublets but leaves the singlets unchanged, whereas the $U(1)$ gauge group transforms the singlet states. The group symmetry that fulfils the desired gauge invariance is the combined $\mathrm{SU}(2)_L \otimes \mathrm{U}(1)_Y$ symmetry group, which represents the electroweak unification in the GSW-model. The index L refers to the LH doublets and the index Y is an abbreviation for hypercharge, with the definition of the hypercharge of

$$Y = 2(Q - T_3), \tag{2.4}$$

where Q is the EM charge and T_3 is the so-called weak isospin [2]. In the EW model, the physical gauge boson fields of the weak and EM interaction are combined by the gauge fields corresponding to the $\mathrm{SU}(2)_L$ and $\mathrm{U}(1)_Y$ group. The three gauge fields $W^i_{\mu\nu}$ with $i = 1, 2, 3$ correspond to the $\mathrm{SU}(2)_L$ group and one gauge field for the $\mathrm{U}(1)_Y$ group, named $B_{\mu\nu}$. The photon field A_μ and the electrically neutral Z_μ boson result as mixtures of $W^{(3)}_\mu$ and B_μ with the weak mixing angle θ_W:

$$Z_\mu = -B_\mu \cos\theta_W + W^{(3)}_\mu \sin\theta_W, \tag{2.5}$$

$$A_\mu = +B_\mu \cos\theta_W + W^{(3)}_\mu \sin\theta_W. \tag{2.6}$$

The two charged $W^\pm$ bosons merge from the combination of $W^{(1)}_\mu$ and $W^{(2)}_\mu$:

$$W^\pm_\mu = \frac{1}{\sqrt{2}}(W^{(1)}_\mu \mp W^{(2)}_\mu). \tag{2.7}$$

So far, the chosen $\mathrm{SU}(2)_L \otimes \mathrm{U}(1)_Y$ gauge symmetry of the EW theory seems to describe all aspects of the interaction well. However, there is one aspect that is not regarded by the formulation of the model yet. Mass terms for the massive gauge bosons can not occur in a gauge invariant Lagrangian. Through spontaneous symmetry breaking (SSB) masses are induced, where the lowest energy (vacuum) state does not respect the gauge symmetry [13]. In the succeeding, the concept of

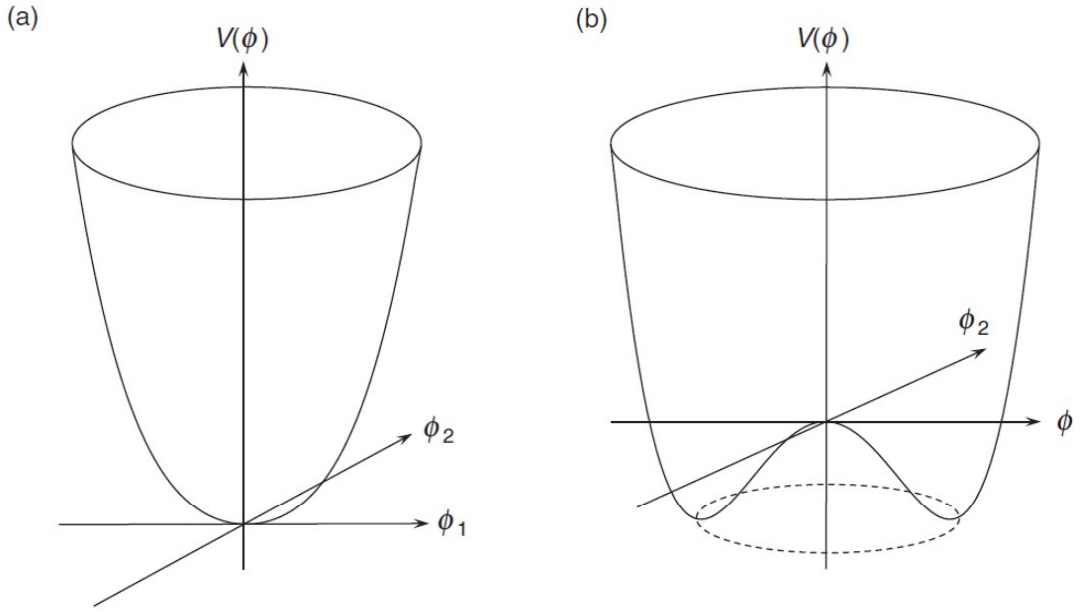

Figure 2.1: The potential $V(\phi)$ for a complex scalar field $\phi = \frac{1}{\sqrt{2}}(\phi_1 + i\phi_2)$ introduced in the Lagrangian for the Higgs mechanism, with (a) $\mu^2 > 0$ and (b) $\mu^2 < 0$ forming the so-called Mexican hat potential [2].

SSB and the Higgs mechanism is introduced following the references [12] and [14]. A solution to this problem is provided by the Higgs mechanism by introducing a complex scalar field ϕ to the Lagrangian

$$\mathcal{L} = (\partial_\mu \phi)^\dagger (\partial^\mu \phi) - V(\phi). \tag{2.8}$$

The potential $V(\phi)$ of the scalar field is formulated as:

$$V(\phi) = \mu^2 |\phi|^2 + \lambda |\phi|^4, \tag{2.9}$$

whereby the form of the potential is dependent on the variable μ^2 for $\lambda > 0$. For the potential $V(\phi)$ shown in Figure 2.1,(a) for $\mu^2 > 0$ a minimum occurs when both fields are zero. Thus, the Lagrangian in Equation 2.8 preserves its global $U(1)$ symmetry. For $\mu^2 < 0$ (Figure 2.1, (b)), the potential has a local maximum at $|\phi| = 0$ and a global minimum at $|\phi| = v^2$. The global minimum is forming a non-zero vacuum expectation value (VEV) with an infinite number of degenerate states at energy v. Choosing one of these states, spontaneously breaks the global $U(1)$ symmetry of the Lagrangian. The evaluation around the VEV of the Lagrangian in Equation 2.8 results in one massive and three massless fields. The massless fields represents

the so-called the Goldstone bosons [15]. These bosons correspond to excitations in the direction, where the potential does not change. The resulting massive field corresponds to the Higgs boson. To identify the mass terms in the Lagrangian in Equation 2.8, the derivatives are replaced with the appropriate covariant derivatives D_μ. The new Lagrangian becomes

$$\mathcal{L}_{\text{Higgs}} = (D_\mu\phi)^\dagger(D^\mu\phi) - \mu^2\phi^\dagger\phi + \lambda(\phi^\dagger\phi)^2, \tag{2.10}$$

$$\partial_\mu \rightarrow D_\mu = (\partial_\mu - igW_\mu - ig'B_\mu). \tag{2.11}$$

Evaluating $\mathcal{L}_{\text{Higgs}}$ in Equation 2.10 around the minimum of the potential results the mass terms of the $W^\pm$ and Z gauge bosons

$$M_W = \frac{vg}{2}, \qquad M_Z = \frac{vg}{2\sqrt{2}cos\theta_W}, \tag{2.12}$$

with the coupling constant g and the weak mixing angle θ_W. The Higgs mechanism can also be used to generate the masses of the fermions. The fermion mass term in the Dirac Lagrangian,

$$-m\bar{\psi}\psi = m(\bar{\psi}_L\psi_R + \bar{\psi}_R\psi_L), \tag{2.13}$$

does not respect the gauge symmetry due to the different transformation properties of LH and RH states. The interaction of the Higgs field with the fermion fields are induced in the gauge-invariant Yukawa Lagrangian $\mathcal{L}_{\text{Yukawa}}$. For the first generation of quarks as an example, the Yukawa Lagrangian reads

$$\mathcal{L}_{\text{Yukawa}} = -y_d(\bar{u}_L, \bar{d}_L)\phi d_R - y_u(\bar{u}_L, \bar{d}_L)\phi_c u_R + h.c \tag{2.14}$$

with additional terms from the Hermitian conjugate. The resulting fermion mass term with the so-called the Yukawa coupling y_f is

$$m_f = \frac{y_f}{\sqrt{2}}. \tag{2.15}$$

2.3 Anomalous Gauge Coupling

Self-interaction terms of the vector bosons arise in the EW model due to the underlying non-abelian gauge theory. These self-interaction terms lead to triple and quartic gauge bosons couplings. The SM predictions from the unified EW model allow triple gauge couplings (TGC) for $W^+W^-\gamma$ and W^+W^-Z and quartic gauge

couplings (QGC) for $W^+W^-W^+W^-$, W^+W^-ZZ and $W^+W^-\gamma\gamma$ [2]. Neutral couplings in production processes as in the ZZZ final states studied in this thesis are forbidden in the SM. The effective field theory (EFT) is a model-independent way of expressing high energy extensions of the Standard Model [16].

New physics can appear as new interactions that are induced in the Lagrangian as higher dimensional operators. These new interactions need to fulfil the SM gauge symmetry of $SU(3)_C \otimes SU(2)_L \otimes U(1)_Y$. The EFT approach includes additional operators of $d > 4$ since the SM fields have mass-dimensions of $d \leq 4$. These operators are satisfying the SM gauge symmetry and are included in the effective Lagrangian $\mathcal{L}_{eff}$ by [17]

$$\mathcal{L}_{eff} = \mathcal{L}_{SM} + \sum_{d>4} \sum_{i} \frac{f_i}{\Lambda^{d-4}} \mathcal{O}_i. \tag{2.16}$$

All operators $\mathcal{O}_i$ at dimension d are summed over, whereby only operators of even dimensions, i.e. $d \in 6, 8, ...$ are involved. Odd dimensional operators would violate baryon and lepton conservation. The coupling operators $\mathcal{O}_i$ have a respective coupling strength determined by the dimensionless coupling parameter f_i. The largest contribution is provided by the dimension-6 operators as they are suppressed by the energy scale Λ^2. The next higher order are the dimension-8 operators, which are already suppressed by Λ^4. Thus, higher energy contributions vanish in the limit of $\Lambda \to \infty$ and the $\mathcal{L}_{eff}$ reduces to the SM Lagrangian $\mathcal{L}_{SM}$. The highest impact contribute the dimension-6 operators and determine the interaction of three and four electroweak gauge bosons [16].

However, they do not give rise to neutral quartic gauge couplings, which is crucial in the study of ZZZ final states. The lowest order operators inducing these neutral anomalous QGC are the dimension-8 operators, listed in Table 2.3. The vertices of $ZZZZ$, $ZZZA$, $ZZAA$, $ZAAA$, $AAAA$ can be sensitive to the ZZZ production process. Thus, all operators shown in Table 2.3 are relevant for the triple Z boson production. For the study of the $WW\gamma$ final state 14 operators are accessible since these operators describe the $W^+W^-\gamma\gamma$, $W^+W^-Z\gamma$ vertices.

Table 2.3: Dimension-8 operators and their relation to the quartic gauge vertices. The marker "X" indicates vertices that are affected by a dimension-8 operator [17].

	WWWW	WWZZ	ZZZZ	WWAZ	WWAA	ZZZA	ZZAA	ZAAA	AAAA
$\mathcal{O}_{S,1}$,$\mathcal{O}_{S,2}$	X	X	X	-	-	-	-	-	
$\mathcal{O}_{M,0}$,$\mathcal{O}_{M,1}$,$\mathcal{O}_{M,6}$,$\mathcal{O}_{M,7}$	X	X	X	X	X	X	X	-	-
$\mathcal{O}_{M,2}$,$\mathcal{O}_{M,3}$,$\mathcal{O}_{M,4}$,$\mathcal{O}_{M,5}$	-	X	X	X	X	X	X	-	-
$\mathcal{O}_{T,0}$,$\mathcal{O}_{T,1}$,$\mathcal{O}_{T,2}$	X	X	X	X	X	X	X	X	X
$\mathcal{O}_{T,5}$,$\mathcal{O}_{T,6}$,$\mathcal{O}_{T,7}$	-	X	X	X	X	X	X	X	X
$\mathcal{O}_{T,8}$,$\mathcal{O}_{T,9}$	-	-	X	-	-	X	X	X	X

2.4 Monte Carlo Simulations

Monte Carlo (MC) simulations enable the comparison of theoretical models with experimental data. This is important in the test of the SM and in the search for new physics. The comparison of experimental data with theoretical predictions is not trivial. Experimental effects that could dilute the signal or lead to deviations from theoretical predictions need to be considered. To overcome those difficulties in the comparison process, MC generators are utilized. The MC production process in ATLAS detector has several steps: First, the event generation is performed with a MC generator. This step is followed by the detector simulation and the digitization step. Lastly, the reconstruction of the simulated data is performed [18]. These simulation steps are described in more detail in the succeeding.

Event Generation

The basic working procedure of the MC generators is to separate the events into different stages. The simulation starts from the highest energy scale (short distance) and adds subsequently subprocesses at lower energy scales (longer distance) [19].

An overview of the event simulation is described in following. Protons are composite objects consisting of quarks and gluons. These substructure objects are referred to as partons. Therefore, the collision of two protons is not a pure elastic scattering but instead a combination of many effects. The core of the simulation is the so-called hard process, which is the collision of the constituent partons with high momentum transfer. This hard interaction is evaluated by the calculation of the matrix

element for the specific process. The accelerated partons can generate radiation in form of gluons or photons. The radiation is categorized into Initial-State Radiation (ISR), where the emissions are associated with the two incoming colliding partons, and Final-State Radiation (FSR), where the emissions are associated with outgoing partons. The emitted gluons can again create new particles due to hadronization processes and the radiated photons can produce electron-positron pairs. These processes lead to a shower of new particles, the so-called parton shower [20]. The simulation at this stage is refereed to as parton level or truth level simulation.

Detector Simulation

The next stage is the simulation of the detector response using the GEANT4 [21] simulation framework. The detector simulation evaluates the particle interaction with the detector material, where energy deposits are recorded as hits [18].

Digitization and Reconstruction

The hits from the detector simulation are translated into detector response as raw data objects (RDO) [22]. This procedure is called digitization and is followed by the reconstruction of the particles. The reconstruction process for the objects that are relevant in this thesis is outlined in Chapter 4. At this reconstruction level (reco level) the full simulation chain is completed. The reconstructed data is saved as analysis object data (AOD). Since these data contain all information of the reconstructed particles, it is too large to provide an efficient analysis procedure and need to be split into subsets. These subsets, which are pre-filtered of different information, are referred to as derived AOD formats (DAODs) [23]. The DAODs are further reduced to the most important informations by introducing an object selection in order to increase efficiency. The reduced data leads to the final n-tuples in form of mini AODs (MxAOD). The MxAODs are Root files and can be analyzed in the Root framework [24]. The data formats of AODs and DAODs are used in the second collision data taking campaign (Run 2) of the ATLAS detector. The data taking in Run 3 has begun and a new common data format, PHYS and PHYSLITE is introduced [25]. One of the main purpose of this new data format is to reduce the disk storage significantly. This is especially important in the high-luminosity LHC (HL-LHC) era, which is expected to start in 2029 [26]. With the HL-LHC 3–4 times more proton–proton collisions are delivered to ATLAS per second and efficient data processing is crucial [23].

MC Generators and Samples

For the simulation process described above MC generators are used. The generators that are relevant to this thesis are MadGraph, Pythia and Sherpa. Some MC samples needed in this study are self-generated with the MC generator MadGraph5_aMC@NLO [27]. MadGraph is a matrix element generator, which is combined in the simulation process of this study with the Pythia8 [28] event generator. Pythia8 generator is included in order to perform next-to-leading-order (NLO) calculations in the parton shower. Furthermore, MC samples are included in this thesis that are officially generated by the ATLAS Group with the Sherpa [29] event generator. A summary of all MC samples used in this thesis with the respective MC generators is provided in Table 2.4. For the ZZZ production process one signal sample is used, that is officially produced by the ATLAS Group with Sherpa 2.2.2. The MC samples for the $WW\gamma$ production process are separated into signal samples and background samples. This thesis studies the $WW\gamma$ final states on Run 3 and compares results with an ongoing ATLAS analysis for Run 2 $WW\gamma$ production. Therefore, MC samples on Run 2 are included. These samples are officially produced by the ATLAS Collaboration. At the time this analysis was performed, MC samples for the $WW\gamma$ process on Run 3 were not produced yet. Thus, all Run 3 samples

Table 2.4: List of the MC simulations used in the ZZZ and $WW\gamma$ analysis. The samples marked with "*" are officially produced by the ATLAS Group. The unmarked samples are self-produced for this thesis.

	Process	Run	Generator
Signal	ZZZ	Run 2*	Sherpa 2.2.2
Signal	$WW\gamma$	Run 2*	Sherpa 2.2.11
	$WW\gamma$	Run 3	MadGraph 2.9.9+Pythia8
$WW\gamma$ Background	$tt\gamma$ decay	Run 2*	MadGraph 2.7.3+Pythia8
	$tt\gamma$ prod.	Run 2*	MadGraph 2.7.3+Pythia8
	$Z\gamma$	Run 2*	Sherpa 2.2.11
	$tt\gamma$ decay	Run 3	MadGraph 2.9.9+Pythia8
$WW\gamma$ Background	$tt\gamma$ prod.	Run 3	MadGraph 2.9.9+Pythia8
	$Z\gamma$	Run 3	MadGraph 2.9.9+Pythia8

included in Table 2.4 are self-produced for this study. The generation of the samples is performed with the generator MadGraph5 2.9.9 interfaced with Phythia8. The samples are produced in Run 2 detector configuration for the ATLAS detector but at the Run 3 centre-of-mass energies of 13.6 TeV.

3 Experimental Setup

The Large Hadron Collider (LHC) is the most powerful particle collider currently existing and is operated at CERN (Conseil Européen pour la Recherche Nucléaire). CERN is a European nuclear research centre located near Geneva and was founded in 1951 [30]. The proton-proton collisions studied in this thesis were detected by the ATLAS detector at the LHC. This Chapter provides an overview of the experimental setup. First, the LHC is introduced in Section 3.1. Afterwards, the ATLAS detector with its different sub-components is described in Section 3.2.

3.1 The Large Hadron Collider

The LHC is a circular particle accelerator with two counter rotating beams of hadrons in a 27 km long ring of superconducting magnets [31]. It is built to study the Standard Model of Particle Physics and beyond. The design center of mass energy is 14 TeV. Currently, the LHC is operating at a center-of-mass energy of 13.6 TeV [32].

A magnetic field around the storage ring deflects the proton beam around the ring. To reach high beam energies a strong dipole field is needed, which bends the proton beam around the ring. A beam energy of 7 TeV requires a dipole field strength of 8.3 T, which is provided by superconducting magnets. These magnets operate at 1.9 K and are cooled using super-fluid helium [33]. Before particles, like protons or heavy ions, enter the beam pipes of the LHC, they pass a chain of pre-accelerators. The accelerator complex is shown in Figure 3.1. To generate a proton beam, negative hydrogen ions are used. They are injected into the linear accelerator LINAC 4, where the hydrogen ions are accelerated up to 160 MeV. The electrons of these accelerated ions are removed and only protons are left, which then enter the Proton Synchrotron Booster (PSB). The PSB pushes the protons to 2 GeV before they are injected into the Proton Synchrotron (PS). Leaving the PS at 26 Gev, the protons are sent to the Super Proton Synchrotron (SPS), where they are further accelerated to 450 GeV. Finally, the protons enter the two beam pipes of the LHC and are accelerated up to

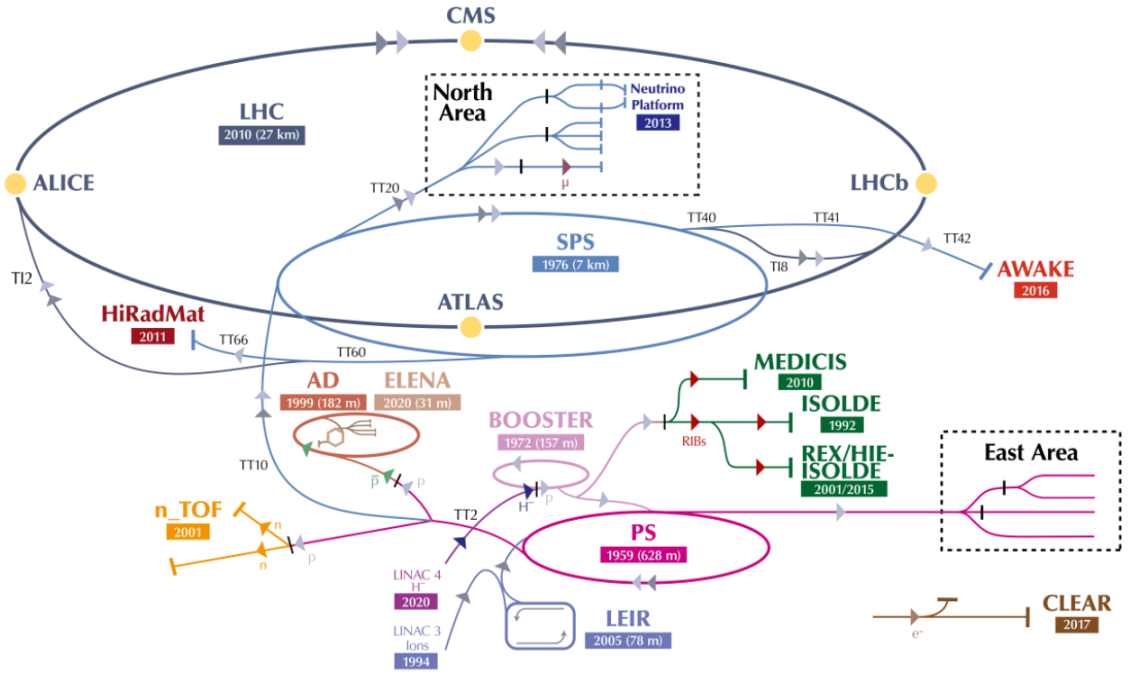

Figure 3.1: The accelerator complex at CERN with the four experiments ATLAS, CMS, ALICE and LHCb located along the LHC ring [34].

6.5 TeV. The two counter-rotating beams intersect at four points with a total energy of 13 Tev [35]. At these interaction points the four main experiments ATLAS, ALICE, CMS and LHCb are located, as shown in Figure 3.1. The ATLAS (A Toroidal Lhc ApparatuS) [36] and the CMS (Compact Muon Solenoid) [37] detectors share the same scientific goals. Both detectors are high luminosity experiments designed to study the SM and physical phenomena beyond [38] but differ in their technical design and magnetic system. The ALICE (A Large Ion Collider Experiment) detector is investigating heavy-ion collisions [39]. The LHCb (Large Hadron Collider beauty) experiment investigates rare decays of hadrons including beauty or charm quarks and study for example the violation of the CP symmetry [40].

Not only high energies are reached at the LHC but also high luminosities. The instantaneous luminosity L is a measure for the number of particle interactions and is expressed as the proportionality factor between the cross section σ and the events per second

$$\frac{dN}{dt} = L \cdot \sigma. \tag{3.1}$$

The total number of events occurring in a period of data taking is calculated by integrating Equation 3.1 over time

$$N_{events} = \sigma \int L dt = \sigma \mathcal{L}. \tag{3.2}$$

where $\mathcal{L}$ is the integrated luminosity [41]. For final states with small cross-section, as investigated in this thesis, a high luminosity is important. Nevertheless, the beam configuration used to obtain high luminosity has its side effects. For example, a higher the number of interacting particles lead to larger contributions of pile-up. The luminosity at the LHC differs for the different experiments. ATLAS and CMS are the two high luminosity experiments. The aim is to reach a peak luminosity of $L = 10^{34}\text{cm}^{-2}\text{s}^{-1}$ for the proton collisions. The experiments LHCb and ALICE are operated at lower luminosities, whereby LHCb is aiming $L = 10^{32}\,\text{cm}^{-2}\text{s}^{-1}$ for b-physics and ALICE peak luminosity is $L = 10^{27}\,\text{cm}^{-2}\text{s}^{-1}$ for lead-lead ion operation [31].

3.2 The ATLAS Experiment

This Chapter describes the ATLAS detector and introduces its sub-detectors. The ATLAS detector is suited in a underground cavern at the LHC. It is a general-purpose detector, which is built to investigate final states of proton-proton and heavy ion interactions. The requirements for the ATLAS detector system have been set by the ATLAS Collaboration and its physics program [42], like the search for the Higgs Boson. Proton-proton collisions investigated at the ATLAS experiment impose the feature of QCD jet production, which dominate over rare processes. Therefore, identifying these processes places demands on particle-identification abilities of the detector.

The coordinate system in the ATLAS detector is defined around the interaction point, which is the origin of the coordinate system. The detector is forward-backward symmetric with respect to the interaction point. The beam direction is parallel to the z-axis and the x-y plane is defined transverse to it. The spherical coordinates are the azimuthal angle ϕ around the beam axis and the polar angle θ from the beam axis.

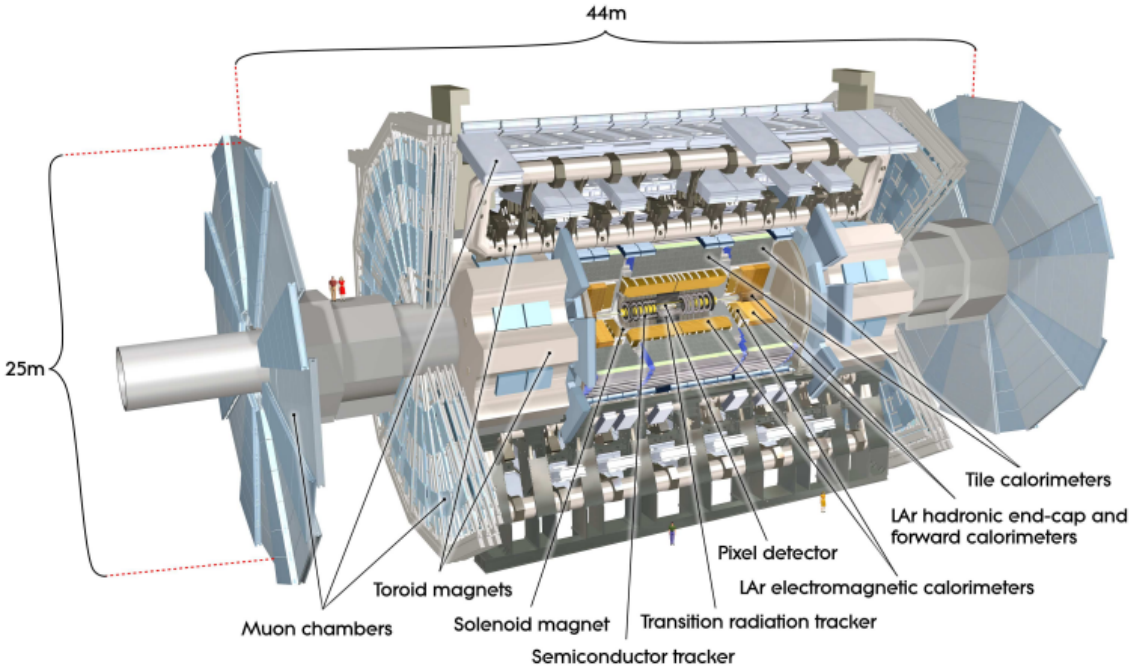

Figure 3.2: Layout of the ATLAS detector with sub-detector components [36].

With the polar angle the pseudorapidity of a particle can be defined as $\eta = -\ln\left(\tan\frac{\theta}{2}\right)$, whereby the distance in the η-ϕ plane is determined with

$$\Delta R = \sqrt{\Delta\eta^2 + \Delta\phi^2}. \tag{3.3}$$

A number of conditions, e.g. high interaction rates and particle multiplicities where taken into account for designing the detector. Essential is a tracking system that provides good momentum resolution and vertex reconstruction. Furthermore a high coverage calorimetry system for electron, photon and hadron identification must be implemented. The high coverage is needed for precise jet and missing transverse momentum measurement. For identifying muons, a good muon system with momentum resolution over a wide range of momenta is required. To reduce the large amount of collision rate and sufficiently reduce background a highly efficient trigger and data acquisition system is needed [36].

The layout of the ATLAS detector is shown in Figure 3.2. The cylindrical shape of the ATLAS detector is 46 m long and has a diameter of 25 m. With a mass of 7000 t it is the heaviest detector ever built for a particle collider. It is arranged in

a barrel shaped central part and two end-caps. The ATLAS detector has different detector systems. In the inner most part is the Inner Detector (ID) located, which is responsible for measuring momentum and trajectory of charged particles. The ID is surrounded by the calorimetry system, which splits up into (LAr) electromagnetic calorimeters, tile calorimeter, LAr hadronic end-cap and forward calorimeter. In the next Section the ID will be described more precisely [36].

3.2.1 The Inner Detector

The ID is located in a solenoidal magnetic field of 2 T. The cylindrical shape consists of a barrel section and two identical end caps, as shown in the Figure 3.3. The ID is designed to reconstruct the tracks and vertices of charged particles and provides excellent momentum resolution. This is given within the pseudorapidity range $|\eta| < 2.5$ [43]. The ID is required to be radiation hard, provide good momentum resolution and have high granularity. Furthermore, the use of material in the ID should be minimal to reduce multiple scattering and ensure a good momentum resolution. There are three complementary sub-detectors, which build up the ID: a Pixel Detector, a Semiconductor Tracker (SCT) and a Transition Radiation Tracker (TRT). The Pixel Detector and SCT are silicon semiconductors and are arranged barrel region around the beam axis, while in the end-cap regions they are located perpendicular to the beam axis. The silicon sensors are operated at low temperatures, -5°C to -10°C, to ensure proper noise performance in this high-radiation region [36].

At the inner radii this high precision tracking system provides excellent pattern recognition. At larger radii the TRT provides continuous tracking over $|\eta| < 2.0$. The TRT is built of gaseous straw tubes interleaved with transition radiation material and provides a large number of trackpoints. The use of a xenon gas mixture in the straws allows the detection of transition photons and the identification of electrons. This technique has less precision compared to the high-precision trackers in the inner part. However, the large number of measurements compensates for the lower precision and the combination of all three detector systems ensures high precision measurements [36].

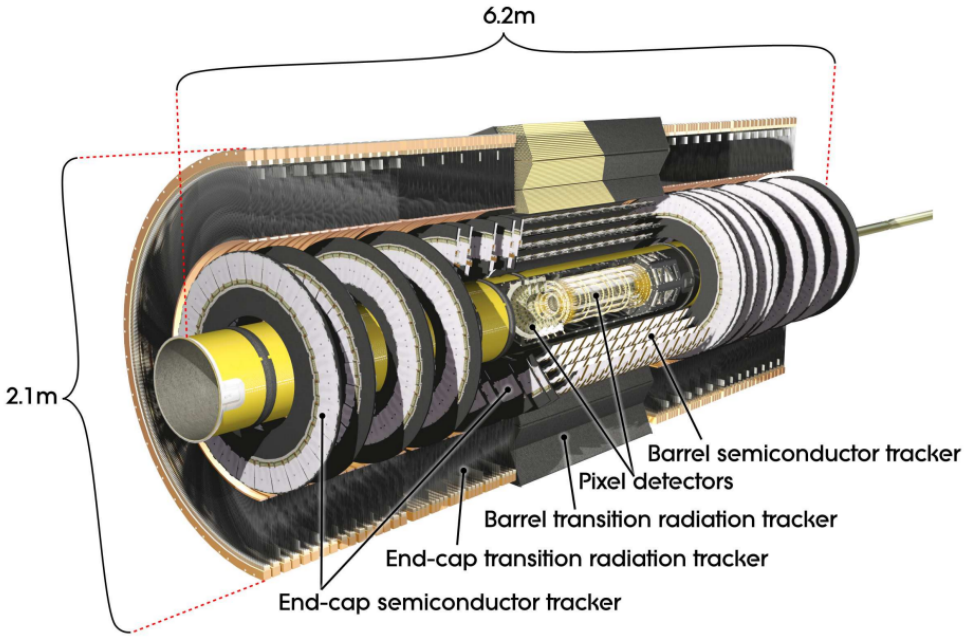

Figure 3.3: Layout of the ATLAS inner detector along with its sub-components depicted [36].

3.2.2 The Magnet System

The magnet system of the ATLAS detector enables measurements of the charge and momentum of charged particles due to magnetic deflection of the particles in the x-y plane. It is built of a solenoid and three large toroids, where the two end cap toroids (ECT) improve the bending power in the high-η region and barrel toroid (BT) covers the central part. The inner most magnet is the central solenoid (CS) surrounding the ID. It is aligned with the beam axis and provides an axial magnetic field of 2 T. The three toroids are positioned with an eight-fold azimuthal symmetry around the calorimeters and are built of eight coils. The toroids provide a toroidal magnetic field of up to 2.5 T and 3.5 T respectively for the muon spectrometer system. The bending power between the barrel and end-cap toroid system is optimized by rotating latter coil system by 22.5 °, which leads to radial overlap [36].

3.2.3 The Muon Spectrometer

The muon spectrometer of the ATLAS detector measures muon tracks due to magnetic deflection and is constructed with stand-alone triggering. The momentum mea-

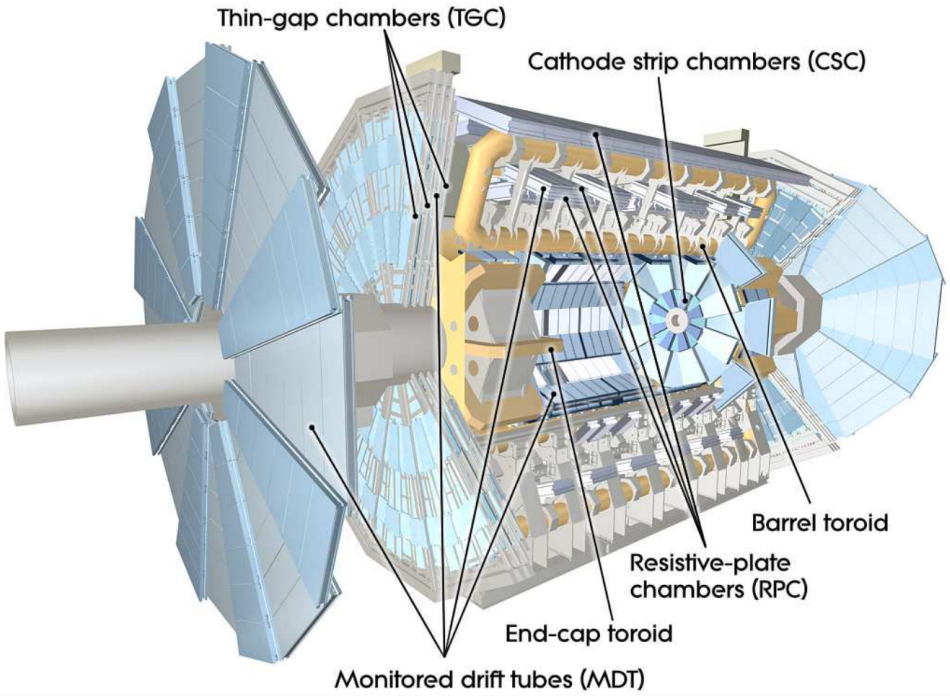

Figure 3.4: Layout of the ATLAS muon spectrometer system with the four different muon chamber types and the toroid magnets shown [36].

surement of the muons expands over a wide range of transverse momentum, pseudorapidity and azimuthal angle. This is achieved by three large superconducting air-core toroid magnets, where the magnetic field is mostly orthogonal to the muon trajectories. The design of the spectrometer is laid out to cope with high particle flux, since parameters like rate capability, granularity, aging properties and radiation hardness are affected [44].

The muon spectrometer is depicted in Figure 3.4. To measure the muon tracks in the barrel region, the large barrel toroid delivers magnetic bending in a range of $|\eta| < 1.4$, where three layers of the chambers are arranged cylindrically around the beam axis. Both ends of the barrel toroid are equipped with end-cap magnets to bent the tracks over $1.6 < |\eta| < 2.7$. The region of $1.4 < |\eta| < 1.6$ is called transition region, where the magnetic fields of the barrel and end-cap magnets ensure magnetic deflection. As in the end-cap region, the chambers are installed in three layers perpendicular to the beam. There are four different kinds of chambers. The Monitored Drift Tubes (MDT's) and the Cathode Strip Chambers (CSC) provide precision tracking of the muon tracks, where MDT cover the largest pseudorapidity range with $|\eta| < 2.7$ and

the CSC deliver measurements at high pseudorapidities in the forward direction, $2 < |\eta| < 2.7$. The CSC reads out tracks with multiwire proportional chambers and provide high granularity to deal with the demanding rates and background conditions in the inner most part. The trigger chambers are the Resistive Plate Chambers (RPC) in the barrel ($|\eta| < 1.4$) and Thin Gap Chambers (TGC) in the end-cap region. The purpose of the trigger system in the muon spectrometer is to measure the transverse momentum and to identify bunch-crossing [36].

3.2.4 The Calorimeters

The calorimeter system in the ATLAS detector is surrounding the ID and is responsible for measuring the energy of particles passing through. There are two components of the calorimeter system. The energy of the passing particles is measured by the electromagnetic calorimeter (ECAL), where as the energy of the hadrons is measured additionally in the hadronic calorimeter (HCAL). The combination of ECAl and HCAL allows precise particle identification. Additionally, the calorimeters must limit punch-through into the muon system and ensure containment for electromagnetic and hadronic showers. This requires an adequate depth of the calorimeter system. Due to the aforementioned properties, high granularity and a large pseudorapidity coverage of $|\eta| < 4.9$, the calorimeters provide a presice measurements for the missing transverse energy variable E^T_{miss}. [36].

The ECAl consists of a barrel part ($|\eta| < 1.47$) and two end-caps ($1.37 < |\eta| < 3.2$). In the barrel region, Liquid Argon (LAr) is used as active material and lead as absorbing material. Particles passing through the absorbing material can produce a particle shower. This process ionizes the active material and produces an electrical current that is measured [45]. The barrel calorimeter is separated by a small gap at $z = 0$ into two identical parts. Each end-cap calorimeter is mechanically divided into two coaxial wheels: an outer wheel covering the region $1.375 < |\eta| < 2.5$ and an inner wheel covering the region $2.5 < |\eta| < 3.2$. Furthermore, a complete ϕ-symmetry is provided due to the accordion geometry. The HCAL extends around the EM calorimeters. The tile calorimeter is placed in the barrel and extended barrel region with pseudorapidity coverage of $|\eta| < 1.7$. Here, steel is used as absorbing material and scintillating tiles are used as the active material [36].

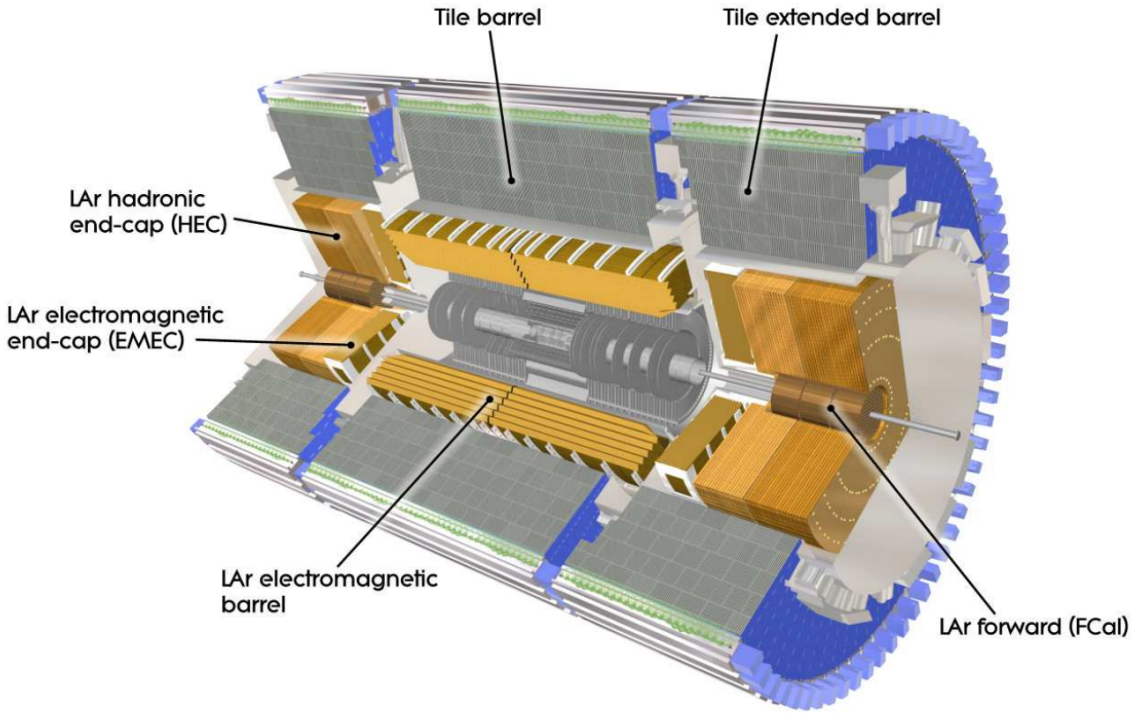

Figure 3.5: Layout of the ATLAS calorimeter system with the electromagnetic and the hadronic detector components [36].

Behind the end-cap EM calorimeter is the LAr hadronic end-cap calorimeter (HEC) is located. It consists of copper plates interleaved with LAr gaps. The pseudorapidity range of the HEC slightly overlaps with that of the tile calorimeter and the forward calorimeter (FCAL) to reduce drop in material density. The FCAL is located in the end-cap cyrostats and is divided into three modules in each end-cap. The first one is made of copper and is designed for electromagnetic measurements and the remaining two are made of tungsten and are responsible for measuring hadronic interactions [36].

3.2.5 Trigger and Data Acquisition

At the ATLAS detector proton bunches collide at a rate of 40 MHz. The ATLAS trigger system employs a two-level trigger system to select the interesting events and reduce the event recording to 1 kHz. The first trigger level is the Level-1 (L1) trigger, which is a hardware-based system that uses information from the calorimeter and muon spectrometer. The L1 calorimeter trigger (L1Calo) reads out and processes the information from the calorimeter. Hereby, a Cluster Processor (CP) and a Jet/Energy-sum Processor (JEP) is used to identify electron, photon, tau and

jet candidates that satisfy an defined energy threshold and additionally determine the missing transverse energy. The L1 muon (L1Muon) trigger processes coincident hits from the RPCs and TGCs to determine muon candidates. The information from L1Calo and L1Muon systems are combined in the Level-1 topological trigger (L1Topo). The L1Topo estimates topological requirements of the objects like invariant masses or angular distances. The information from all sub-components of the L1 trigger system is transferred to the central trigger processor (CTP), where the final trigger decision is formed. The triggering procedure in the L1 trigger reduces the event rate to 100 kHz with a processing time of 2.5 μs [46].

The L1 trigger system additionally identifies regions-of-interest (RoIs) within the η-ϕ-space, which is investigated by the second trigger stage. The second stage of the trigger is a software-based trigger, called High-Level Trigger (HLT), which is using the full granularity detector information for selection algorithms. The used information is either the RoI or the full detector information. The HLT reduces the event rate to approximately 1 kHz within a decision time of about 200 ms [47]. The events accepted by the HLT are stored for offline reconstruction and exported at a CERN computing centre, where the data information is further processed [46].

4 Object Reconstruction

The objects produced in particle collisions leave specific signatures in the detector systems. Those characteristic signals are processed and the respective particles are reconstructed. The reconstruction process of all particles relevant in the analysis of the ZZZ and $WW\gamma$ final states is outlined in the following. In the first Section 4.1 the reconstruction of electrons and photons are described. This is followed by a detailed description of muons and missing transverse energy in section 4.2 and 4.3, respectively.

4.1 Electrons and Photons

Distinguishing electrons from photons requires special care due to their similar signature in the detector. The sub-detector systems used in the reconstruction of those particles are the electromagnetic calorimeter and the inner detector. In the calorimeter, electromagnetic objects interact with the detector material, resulting in electromagnetic showers and resulting energy clusters. For electrons, an additional track in the ID is required to match the position and energy of the cluster in the calorimeter [48]. However, this matching process is not always straightforward. The electron can lead to Bremsstrahlung when interacting with the detector material and the radiated photon can convert to electron-positron pair production. These photons are called converted photons. In the electromagnetic calorimeter these shower-particles are usually reconstructed within the same cluster, whereas in the inner detector these particles can cause multiple tracks. Thus, it is possible to match one electromagnetic cluster to multiple tracks that are originated from one primary electron [49].

No tracks are required for photons in the ID except for converted photons. These converted photons are categorized in single-track and double-track. Single-track converted photons are reconstructed as one track without any hits in the innermost layers of the tracking detector. Double-track converted photons on the other hand, emerge from two tracks of the same vertex that belong to a electromagnetically neu-

tral particle. An unconverted photon is a cluster in the electromagnetic system that does not correspond to either a conversion or an electron track [50].

It is possible to misidentify objects in the reconstruction process. These misidentified objects are excluded by applying isolation and identification working points (WP). In general, the WPs are categorized into three different levels: *loose*, *medium* and *tight*. The design of these levels are such that the tight level contains the medium level, and the medium level fully contains the loose level. The tighter the identification level is the more background gets rejected [51]. There are two main identification methods used for electrons. The first one is a cut-based identification, which is based on sequential cuts on selected track and shower variables. The second one is a likelihood approach. Latter method is chosen for electrons, because of its simple construction. To classify if an object is coming from the signal or the background, an overall probability is calculated by using probability density functions (PDF's) and combining them into a discriminant $d_{\mathcal{L}}$ [52]:

$$d_{\mathcal{L}} = \frac{\mathcal{L}_S}{\mathcal{L}_S + \mathcal{L}_B}, \qquad \mathcal{L}_S(\vec{x}) = \prod_{i=1}^{n} P_{s,i}(x_i), \tag{4.1}$$

where $P_{s,i}(x_i)$ is the signal PDF and $\vec{x}$ is the vector of the variable values. The background PDF $P_{b,i}(x_i)$ is calculated the in same manner as in Equation 4.1. For photons the identification requires a high signal efficiency and background rejection to distinguish prompt photons from background photons. In addition to the identification requirements, isolation requirements are made for electrons and photons to further minimize misidentification. The Isolation WP require low activity around a cone-shaped area of the particle-trajectory. The calorimeter-based isolation is a measure for the sum of the transverse energy deposited in the calorimeter cells within a cone of ΔR around the electron. The track-based isolation is the sum of the transverse momentum of the tracks around the particle within a cone of radius ΔR. The isolation measurement only considers tracks that are coming from the primary vertex associated to the particle track [53].

4.2 Muons

The primary signature of muons, as a minimum-ionizing particles, are tracks in the muon spectrometer in combination with tracks in the ID. Starting from the muon spectrometer, track segments are reconstructed from hits in each layer and combined into muon-candidate tracks. Different muon reconstruction algorithms then combine the information from the muon spectrometer, the inner detector and the calorimeter. These algorithms mainly perform a global refit of the tracks in the muon spectrometer, while hits in the muon spectrometer can be added or removed to increase the track quality. Muons identified by matching muon spectrometer tracks with the ID tracks are called combined muons. A complementary method defines inside-out muons, where tracks in the ID are matched to at least three tracks in the muon spectrometer. In both methods the energy loss in the calorimeters are taken into account to combine the track-fit. When the energy depositions in the calorimters are combined with single tracks in the ID, the so-called calorimeter-tagged muons are reconstructed. Segmented-tagged muons are identified by extrapolating a muon track in the ID to a single hit in the muon spectrometer by satisfying tight angular matching. Extrapolated muons are defined when no track from the muon spectrometer can be matched to the ID. This can occur if the muons exploit the full η-coverage of the muon spectrometer of $|\eta| = 2.7$ and thus exceed outside the acceptance of the ID [54].

To reduce misidentification isolation and identification WPs are applied, which are divided into loose, medium, and tight. Isolation requirements are applied to differentiate prompt muons from non-prompt muons. These non-prompt muons are coming from hadronic sources and are accompanied by other charged particles. There are different ways to measure the muon isolation. The track-based isolation works with tracks in the ID and is defined as the sum of the track-p_T's in a cone of size ΔR around the muon. Isolation measurements using the cell clusters in the calorimeter within a cone of size ΔR around the muon, are called calorimeter-based isolation. In both cases the transverse momentum contribution from the muon is subtracted. Comparing both methods, the track-based isolation delivers better resolution and lower pile-up dependence and the calorimeter-based isolation takes neutral particles into account, which would be discarded in the track isolation. The combined information of both isolation measurements methods is called particle-flow-based isolation and provides the best results [55].

4.3 Missing Transverse Energy

Momentum conservation in collider experiments implies that the summed transverse momentum of the colliding objects in the transverse plane should cancel. A measure for any imbalance in the transverse plane is known as missing transverse momentum, or E_T^{miss}. This quantity is especially important for the $WW\gamma$ production process since neutrinos are part of the signal, which do not interact with the detector. However, they carry energy and can be detected indirectly trough momentum imbalance in the transverse plane. Other effects that may lead to an energy imbalance are detector effects that distort the energy measurement, insufficient reconstructed particles or jets. Jets can lead to missing transverse energy, as they are composed of many hadrons that are tightly bundled in energy clusters. Some of these hadrons may not be reconstructed properly and lead to unfulfilled conversion of energy. The total transverse energy imbalance in the x-direction (y-direction) is

$$E_{x(y)}^{miss} = E_{x(y)}^{miss,e} + E_{x(y)}^{miss,\gamma} + E_{x(y)}^{miss,\tau} + E_{x(y)}^{miss,jets} + E_{x(y)}^{miss,\mu} + E_{x(y)}^{miss,soft}. \tag{4.2}$$

For each object in Equation 4.3 the respective term is defined as the negative vectorial sum of the momenta. The E_T^{miss} reconstruction process uses calorimeter cells that are calibrated according to the reconstructed objects they are associated with. This association occurs in a given order to avoid overlap between the objects: electrons, photons, hadronically decaying τ-leptons, jets and then muons. Energy clusters that are not associated with any physical objects are collected in the so-called soft term $E_{x(y)}^{miss,soft}$. The total missing transverse energy E_T^{miss} is calculated as

$$E_T^{miss} = \sqrt{(E_x^{miss})^2 + (E_y^{miss})^2}. \tag{4.3}$$

The process of reconstructing E_T^{miss} is very vulnerable to pile-up effects. Pile-up originating from interactions from other bunch crossings, as well as pile-up from additional proton-proton collisions in the same bunch crossing, can affect the reconstruction. Therefore, the hard term is fully calibrated and corrected for pile-up and several correction methods are applied to the soft term [56].

5 Analysis of the ZZZ final state

Electroweak production of triboson states are among the rarest processes measured with the ATLAS detector and require a large dataset to achieve sensitivity. Yet, deeper insights into those production processes are important to test the non-abelian gauge structure of the SM and to search for new physics at higher energy scales. The triple gauge boson production of ZZZ is studied in this Chapter for a full Run 2 MC dataset. The ATLAS detector recorded the Run 2 proton–proton collisions between 2015 and 2018 at $\sqrt{s} = 13\,\text{TeV}$ with an integrated luminosity of $\mathcal{L}_{int} = 140\ \text{fb}^{-1}$.

In the beginning of this Chapter, the signature of the ZZZ production process is defined in Section 5.1 and the corresponding object and event selection criteria are described in Section 5.2. The analysis prospects of the ZZZ final states are outlined in Section 5.3. Here, the kinematic properties and possible background processes are discussed and the expected number of signal events is presented.

5.1 Signal Definition

The Z boson is an unstable particle and is reconstructed via its decay products in the detector. The decay products are always a pair of a particle and an antiparticle, since the Z boson has zero electrical charge. Hadronic decays have the highest branching ratio (Br) of $Br(Z \rightarrow \text{hadrons}) = 69.9\%$, followed by the decay into two neutrinos with $Br(Z \rightarrow \nu\bar{\nu}) = 20.0\%$. The least probable decay mode is the leptonic decay with $Br(Z \rightarrow l^+l^-) = 10.0\%$ [57].

To select the most suitable signal for this study, following aspects are taken into consideration. Neutrinos do not leave a signal in the detector and can only be detected indirectly. For the hadronic decay channel, large QCD-backgrounds are present and dilute the signal. Despite dealing with low statistics in the lepton channel, it provides the cleanest signal in the detector. Therefore, a purely leptonic signature is chosen

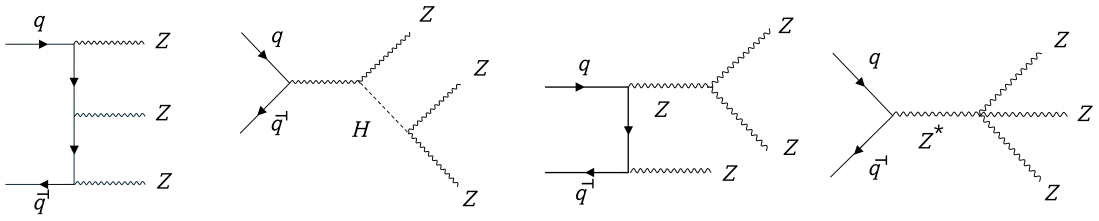

Figure 5.1: Feynman diagrams for the ZZZ production process in leading order (LO). The first two Feynman diagrams show the production of three Z bosons with normal coupling. The third diagram shows the production involving anomalous TGC and the in the last diagram, the production involving the anomalous QGC vertex is presented.

and the signal of interest consists of three lepton pairs, each with opposite-sign and same-flavor (OSSF) leptons: $ZZZ \rightarrow 3(l^{\pm}l^{\mp})$, where $l = (e, \mu)$. The production of three Z bosons at leading order (LO) can originate for example from processes shown in Figure 5.1. The first Feynman diagram shows a production process, where each Z boson is radiated directly from quarks, without involving any interactions between electroweak force carriers. In the second diagram, an intermediate Higgs boson is produced, which decays into two Z bosons. The following two Feynman diagrams are illustrating the ZZZ final state production via anomalous triple gauge coupling (TGC) and anomalous quartic gauge coupling (QGC), respectively. The anomalous coupling of three neutral gauge bosons would violate the underlying $\mathrm{SU}(2)_L \times \mathrm{U}(1)_\mathrm{Y}$ symmetry of the SM. However, in the high-energy scales of the SM, these couplings can exist in some extension [58]. Anomalous couplings in the SM are described in more detail in Chapter 2.

5.2 Object and Event Selection

The production of a ZZZ triboson state is a rare process with a low cross-section. Therefore, it is crucial to apply tight selection criteria on the final state objects and their kinematic variables to reject possible backgrounds from more likely processes. The selection criteria are applied in two sequential steps. First, a pre-selection is performed while generating MxAODs, which is a data format of optimized and reduced information to achieve efficient evaluation of the dataset described in more detail in Section 2.4. This pre-selection, also known as object selection, is set to identify

interesting objects to the analysis and reduce the amount of data. Additional selection requirements are applied in the event selection to define the phase space of the analysis and place further requirements on the signal. In the following, the procedure of object and event selection is described in more detail.

Object Selection

Baseline quality requirements are imposed on electron and muon candidates in the object selection. For all events, good data taking quality must be ensured. This is considered in the so-called Good Run List [59]. All events considered further in the analysis must pass this criteria. In the pre-selection, at least six lepton candidates are requested. These electron and muon candidates must pass medium identification WPs and loose isolation WPs [60,61]. In addition, only electron and muon candidates passing the transverse momentum threshold of $p_T > 7\,\text{GeV}$ are considered further. This minimum transverse momentum requirement is set due to detector limits [62]. Electrons are reconstructed within $|\eta| < 2.47$, whereby the pseudorapidity range of $1.37 < |\eta| < 1.52$ must be excluded due to the transition region between the barrel and end-cap of the electromagnetic calorimeter. The energy resolution of electrons in this transition region is poorly due to the high amount of passive material [63]. Muons are required to be reconstructed in the pseudorapidity range of $|\eta| < 2.5$. The ID information is available in this region in addition to the muon detector information.

All six leptons are required to originate from the primary vertex (PV), which is the vertex with the highest squared transverse momenta $\sum(p_T^2)$ of the associated tracks. Transverse (d_0) and longitudinal (z_0) impact parameters of tracks are defined with respect to the PV. The longitudinal parameter is a measure for the distance between the lepton track and the primary vertex along the beamline. Calculated relative to the primary vertex and multiplied by $\sin\theta$ of the track, the longitudinal impact parameter is required to fulfil $|\Delta z_0 \sin\theta| < 0.5$ mm for electron and muon tracks. The transverse impact parameter d_0 is a measure for the distance between the lepton track and the primary vertex in the transverse plane. To be further considered, electrons and muons must satisfy $|\Delta d_0/\sigma_{d_0}| < 5.0$ and < 3.0, respectively, with σ_{d_0} being the estimated uncertainty of d_0 [64]. In the ID of the ATLAS detector, the same hits can be reconstructed as multiple objects. In the calorimeter, a single cluster can be attributed to an electron as well as a photon candidate. Hence, a so called overlap

removal is performed to remove nearby located objects in the ΔR-space. In the pre-selection, electrons are removed if their distance to muons is $\Delta R(e, \mu) < 0.2$. A summary of all object selection criteria is provided in Table 5.1 along with the event selection requirements, which are described in the following.

Table 5.1: Object selection and event selection of the ZZZ signal region.

	Requirements
Leptons	Leading lepton: $p_T > 30\,\text{GeV}$
	Remaining leptons: $p_T > 10\,\text{GeV}$
Electrons	Loose isolation
	Tight ID (l_1), Medium ID (l_i)
	$\lvert\eta\rvert < 2.47$, excluded $1.37 < \lvert\eta\rvert < 1.52$
	$\lvert\Delta d_0/\sigma_{d_0}\rvert < 5.0$, $\lvert\Delta z_0 \sin\theta\rvert < 0.5$mm
Muons	Medium ID
	Tight iso (l_1), Loose iso (l_i)
	$\lvert\eta\rvert < 2.5$
	$\lvert\Delta d_0/\sigma_{d_0}\rvert < 3.0$, $\lvert\Delta z_0 \sin\theta\rvert < 0.5$mm
Multiplicity	≥ 3 OSSF lepton pairs
Overlap removal	$\Delta R(e, \mu) > 0.2$
Invariant Mass	$m_{ll} > 40$GeV for all pairs
	$\min(\lvert m_{ll,1} - m_Z\rvert + \lvert m_{ll,2} - m_Z\rvert + \lvert m_{ll,3} - m_Z\rvert)$

Event Selection

The event selection defines the phase space of this analysis. Further requirements are placed to receive a signal enriched region in the dataset. For this analysis, only the purely leptonic decay channel of the Z boson is considered, as explained in Section 5.1. The signal is a combination of three OSSF lepton pairs, composed of either two electrons or two muons. To combine the six signal leptons into the correct OSSF lepton pairs of each Z boson is crucial in the selection process. For example, in an event with six same flavour leptons, there are six possible combinations in order to generate three pairs of OSSF leptons. The algorithm to achieve that is explained in the following: First, in a loop over all leptons generates pairs with opposite charge

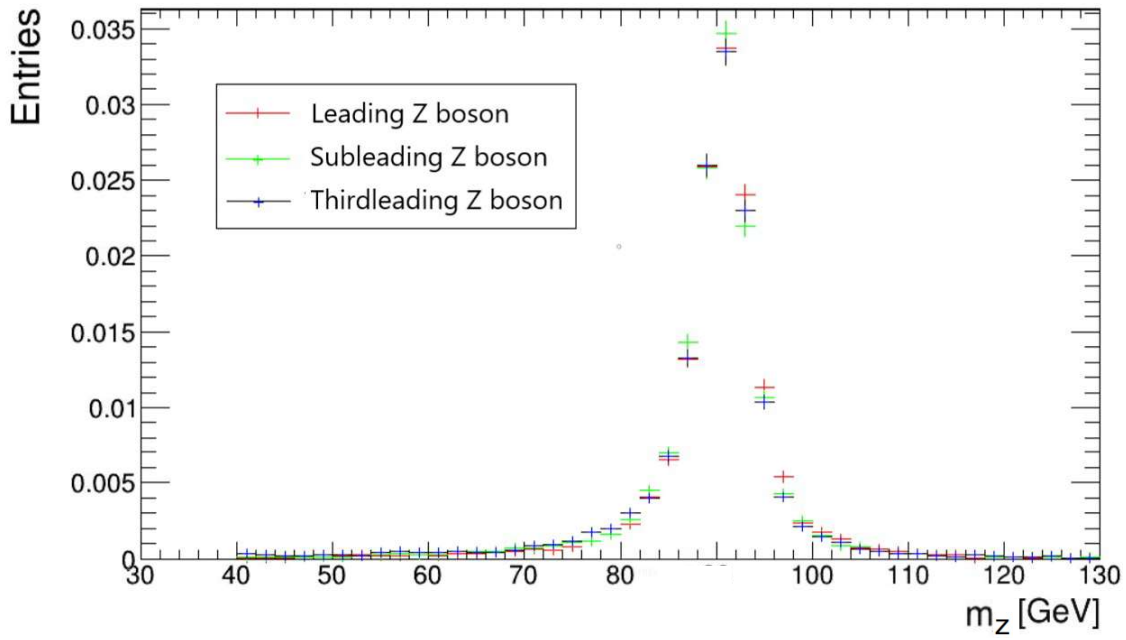

Figure 5.2: Invariant mass distribution of the three Z bosons, where the leading Z boson is depicted in red, the subleading in green and the thirdleading in blue.

and opposite flavour. An invariant dilepton mass of at least $m_{ll} > 40\,\text{GeV}$ is required for these pairs in order to reject low mass resonances (e.g. J/Ψ [65]). From the remaining pairs, the specific three pairs are combined as signal that are closest to the mass of three Z bosons:

$$\min(|m_{ll,1} - m_Z| + |m_{ll,2} - m_Z| + |m_{ll,3} - m_Z|). \tag{5.1}$$

After creating and selecting the most suitable pairs, they are sorted by their transverse momentum and assigned to their mother Z boson. This is done by also sorting the thee Z bosons by transverse momentum, whereby the leading boson (Z_1) has the highest transverse momentum, the subleading (Z_2) the second highest and the thirdleading (Z_3) boson has the third highest p_T. The invariant mass of all three Z bosons are shown in Figure 5.2. All three distributions show a clean peak at the invariant Z mass of 90 GeV. Furthermore, all leptons are ordered by their transverse momentum. The leading lepton l_1 is the lepton with the highest momentum, the

subleading l_2 has the second highest momentum and so on. The leading lepton is required to have $p_T > 30\,\text{GeV}$ due to the efficiency of the single lepton triggers used in this analysis. The leading lepton must satisfy more restrictive identification and isolation requirements in order to guarantee that the corresponding trigger is fully efficient. If the leading lepton is an electron, tight identification requirements must be met. In case of a muon as leading lepton, a tight isolation WP is required. The transverse momentum requirement for the remaining leptons is chosen to be $p_T > 10\,\text{GeV}$. This minimum p_T requirement serves the purpose of excluding low energy objects that are prone to misidentification.

5.3 Analysis Prospects

This thesis provides a first glimpse into the ZZZ production process for Run 2 energies and the results are outlined in this Section. First, the kinematic properties of the events are explained and possible background effects are discussed afterwards. The event expectation for the signal is presented and discussed at the end.

5.3.1 Event Kinematics

Investigating the transverse momentum distributions and the distribution in the η-ϕ space for the three Z bosons can provide insightful information about the event kinematics. The separation of particles in η-ϕ space is described by the variable $\Delta R = \sqrt{\Delta\eta^2 + \Delta\phi^2}$. The ΔR distributions of the three Z bosons are displayed in the left column of Figure 5.3. The first distribution (a) shows the ΔR distribution between Z_1 and Z_2, the second one (c) between Z_2 and Z_3 and the last one (e) shows Z_3 and Z_1. A clean peak around π can be seen in the first distribution. This indicates that Z_1 and Z_2 are produced back-to-back in the transverse plane. The second distribution for Z_2 and Z_3 depicts lower ΔR values. Thus, these two Z bosons are produced closer to each other. The ΔR between the Z_1 and Z_3 in the last distribution is also peaking around π. The wider peak indicates a smaller separation angle between Z_1 and Z_3 compared to the separation of Z_1 and Z_2. Regarding these results, the structure of the event can be reconstructed as shown in Figure 5.4. The Z_1 boson is boosted in the transverse plane and has the combined transverse momentum of Z_2 and Z_3 due to momentum conservation. This event configuration is also consistent with the transverse momentum distribution of the Z bosons presented in the right column of Figure 5.3, where (b), (d) and (f) correspond to Z_1, Z_2 and

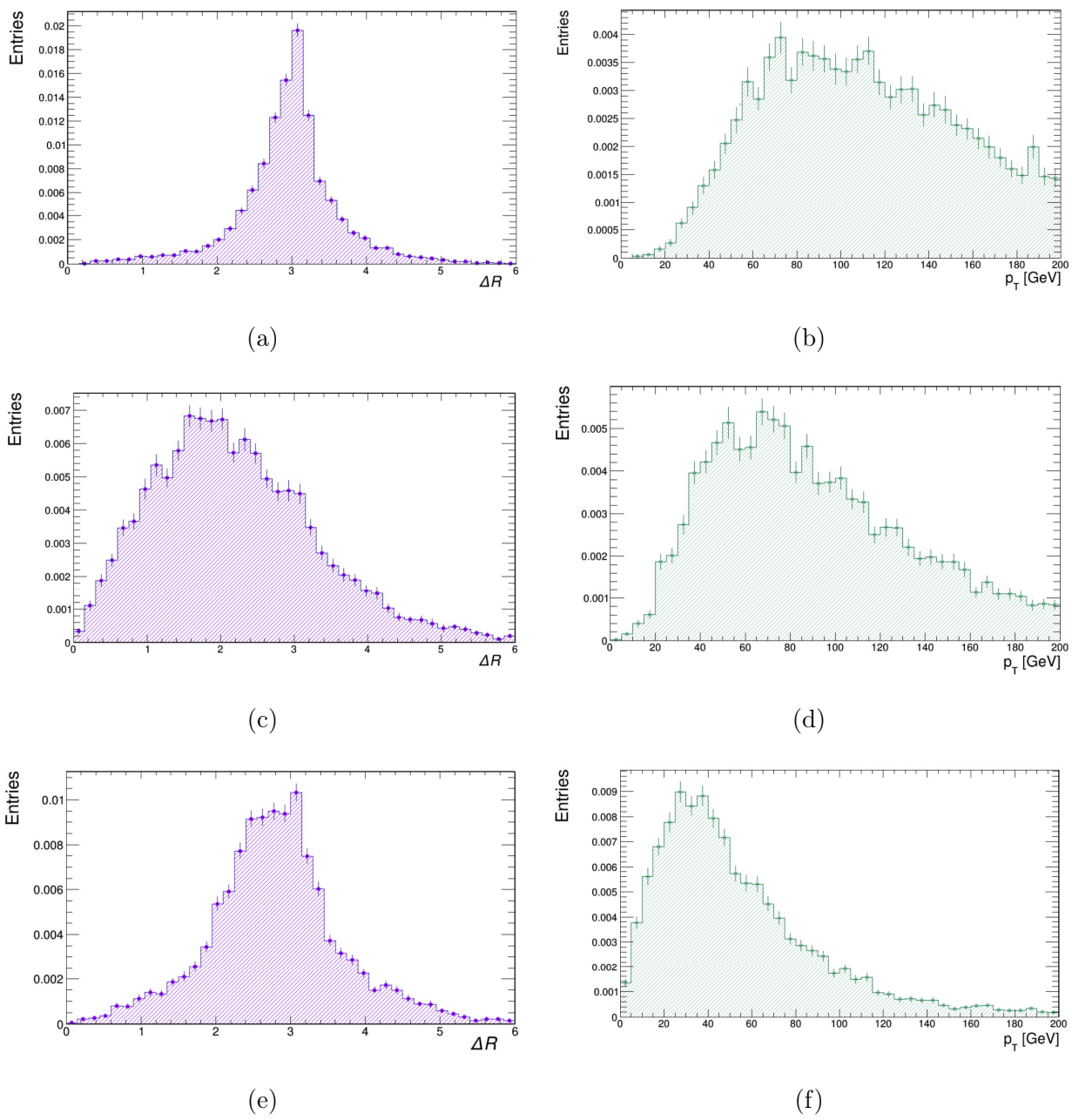

Figure 5.3: The ΔR and transverse momentum distributions of the Z bosons. The left column shows the ΔR distributions between the three Z bosons, where (a) is between Z_1 and Z_2, (c) is between Z_2 and Z_3 and (d) is between Z_1 and Z_3. The right column depicts the transverse momentum distributions of the Z bosons, where (a) is Z_1, (b) is Z_2 and (c) is Z_3.

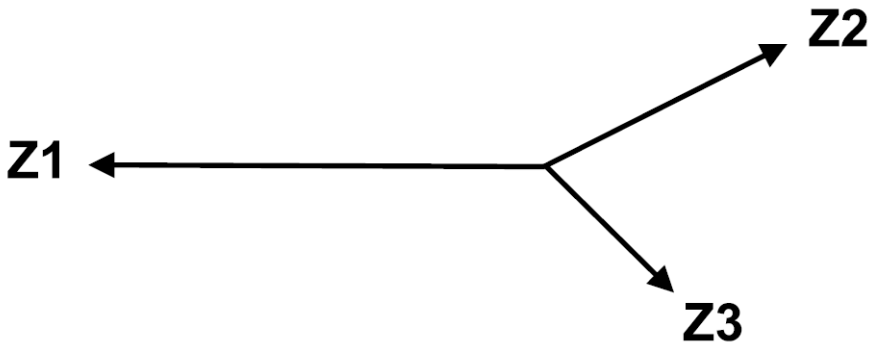

Figure 5.4: Sketch of the resulting distribution of the three Z bosons according to their ΔR distributions, where Z_1 is the leading, Z_2 the subleading and Z_3 the thirdleading boson.

Z_3, respectively. The ΔR distributions of the signal leptons are investigated in the same way as for the Z bosons. Studying the ΔR distributions of the leptons provides insights on how well separated they are in an event. In the reconstruction process of multi-lepton signatures a clean separation between the leptons ensure proper identification. If two prompt leptons are produced to close to each other, one lepton could be missed in the reconstruction process. As an example, events with six electrons are chosen where the electrons are sorted into pairs, as described in Section 5.2. In Figure 5.5, the transverse momentum distributions of the electrons are shown, where the distributions (a),(b) correspond to the two electrons originated from Z_1, (c),(d) to the electrons from Z_2 and (e),(f) correspond to the electrons from Z_3.

The ΔR distributions of these electrons are shown in Figure 5.6. The first distribution (a) depicts the two electrons from the leading Z boson and is peaking at smaller values of ΔR. These leptons have the lowest separation in ΔR-space compared to the other electron pairs. This is due to the high p_T of the leading boson, which results in a boost of the decaying leptons in the same direction. The second and third distributions correspond to the lepton pairs decayed of the subleading and thirdleading Z boson, respectively. The lepton pairs originating from the lower-p_T Z bosons, have a ΔR distribution, which is shifted towards higher values. The highest distance is shown for the electrons from the thirdleading Z boson in (c). They are separated at an angle of roughly π, which indicates that the electrons are produced at rest. The resulting event structure is sketched in Figure 5.7.

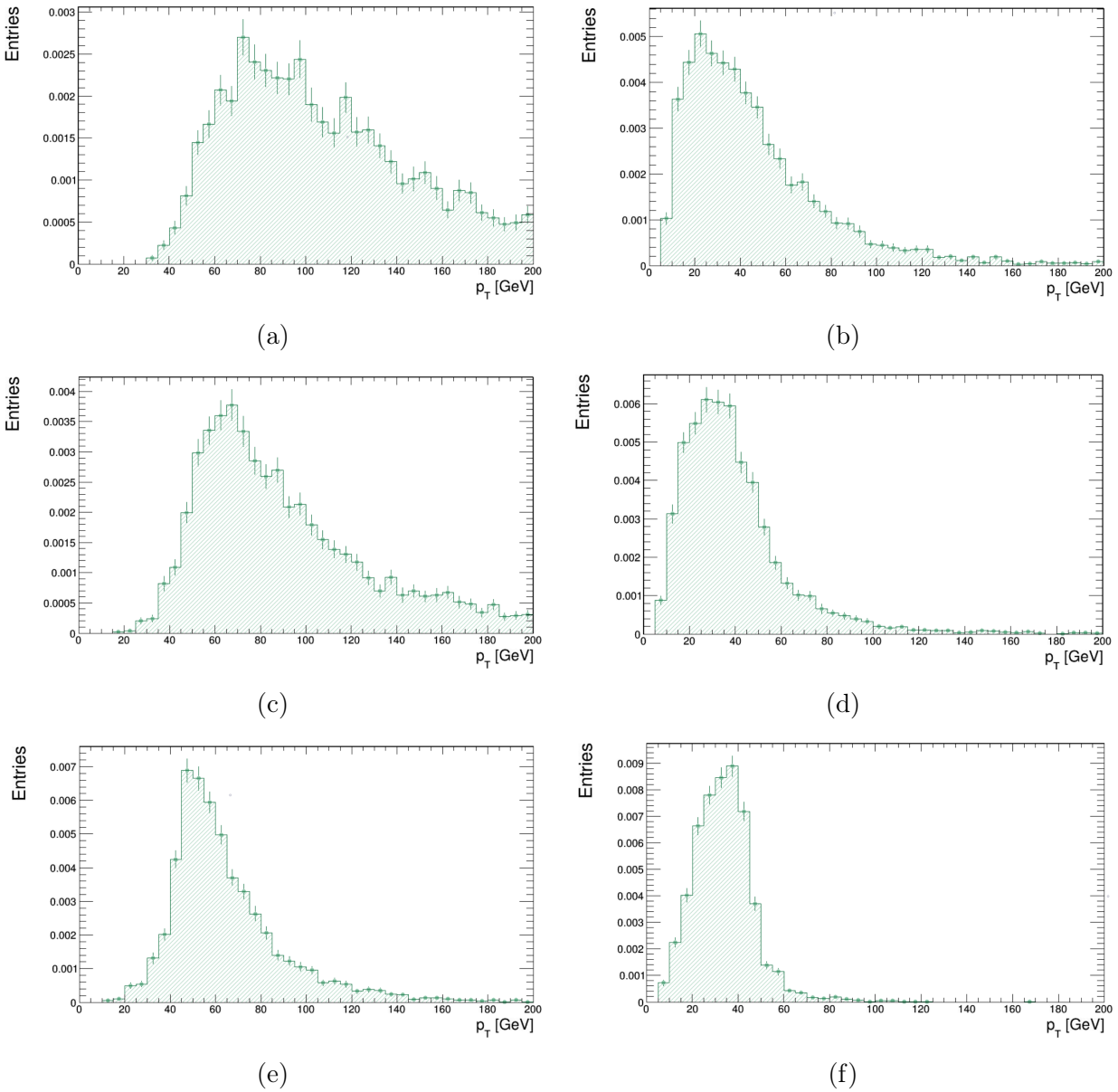

Figure 5.5: The transverse momentum distributions of the six signal electrons, where the distributions (a),(b) correspond to the two electrons originated from Z_1, (c),(d) to the electrons from Z_2 and (e),(f) correspond to the electrons from Z_3.

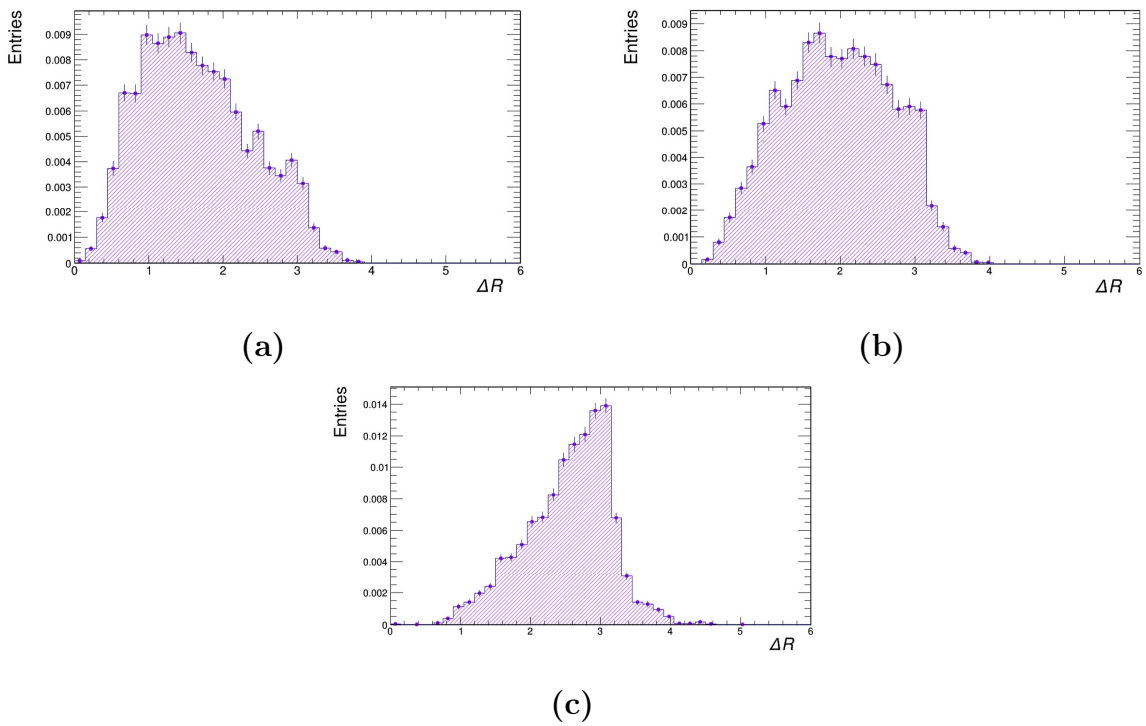

Figure 5.6: The ΔR distributions of the six signal electrons are shown, where (a) depicts the two electrons from the leading Z boson, (b) from the subleading Z boson and (c) from the thirdleading Z boson.

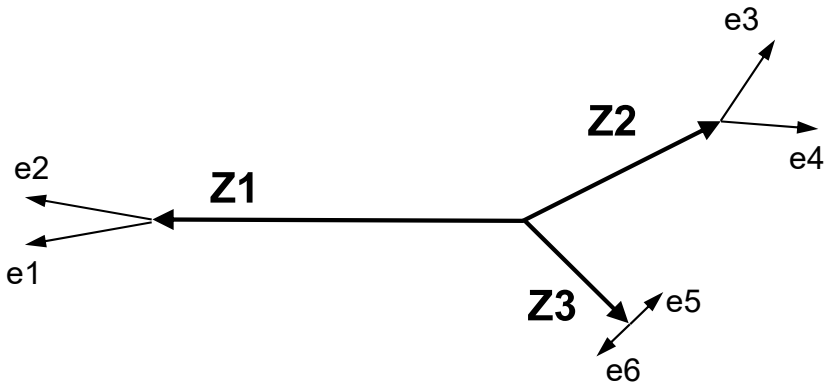

Figure 5.7: Sketch of the resulting distribution of the six signal electrons according to their ΔR distributions.

5.3.2 Background

Due to strict lepton identification and isolation requirements, the leptonic signature of the triple Z boson production is considered as a pure signal of confidently identified leptons. Additional mass requirements are placed to ensure lepton pairs from the Z boson decay. Possible background effects are suppressed in the selection process. In general, the contribution from background processes is considered to be low for the ZZZ final states, since other processes generating a signature of six leptons are rare. For this study, the background is considered to be negligible due to low event yields and the pure signal process, which is further discussed in the following.

Regarding the diboson ZZ process in a previous Run 2 analysis [58], the background contributions are small with approximately 1 % of the predicted signal. This can be considered as an upper limit of background contribution for the triboson process in Run 2. Since the expected event yields in the ZZZ final state are low and the background contribution is considered to be a small fraction of the event yields, the background will be considered as negligible in this analysis. Nonetheless, for higher luminosity experiments in the future, background effects have to be taken into account. For leptonic decaying Z bosons, other processes that could generate a signal of six leptons must be considered.

The so-called irreducible background processes can mimic the signature and have to be distinguished from the signal of interest. In case of the ZZZ final state, only a few processes come into account. The signal could be produced by a $ZZZW$ production process, or a $ZZWW$ process with leptonic decaying W bosons. This quartic gauge boson productions can create a six lepton as signal, but the cross-section for a process including four gauge bosons is even lower than for triboson processes. Other processes, like ZZW, would require an additional lepton. This can occur if other objects, like jets or photons, are falsely identified as leptons, so-called misidentified leptons. Misidentified leptons can also cause the $t\bar{t}Z$ process to contribute to the $3(l^{\pm}l^{\mp})$ final state. Top quarks decay with a branching ratio of about 100 % into a W boson and a b-quark [66]. The two b-quarks could hadronize and create two fake leptons. Additionally, the W bosons can decay into a charged lepton and a corresponding neutrino. With the leptonic decay of the Z boson, this process would generate a signal of six leptons. Those kind of background processes

have to be considered in the future of high luminosity LHC (HL-LHC) and must be subtracted from the sample of selected event candidates. Impacts of the HL-LHC on the ZZZ triboson process are explained in more detail in the next section.

5.3.3 Signal Extraction

The resulting Run 2 event expectation for the ZZZ final state in the purely leptonic decay channel is presented in the following. The results are interpreted in the context of other triboson processes involving the Z boson. Future prospects of analysing the rare ZZZ production process due to the progress of the high luminosity performance of the LHC, is discussed at the end.

The expected number of signal events is predicted using an officially produced ZZZ MC sample by the ATLAS collaboration. The signal sample is generated in Sherpa 2.2.2 with only on-shell contributions and an accuracy of up to NLO QCD precision. The impact of the event selection requirements on the event yield is displayed in the cut-flow diagram in Figure 5.8. The transverse momentum requirement for the leading lepton of $p_T > 30\,\text{GeV}$ slightly reduces the event number. This result is as expected, since the leading leptons have high p_T. The cut-flow diagram reveals that the p_T-requirements on the remaining leptons have no impact on the event yield.

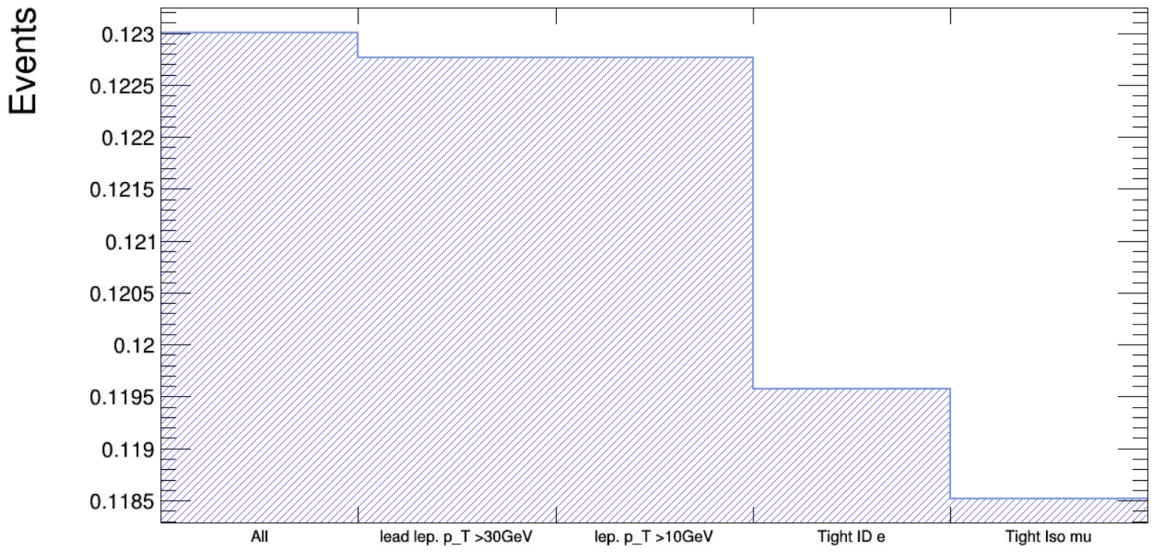

Figure 5.8: The cut-flow diagram for the selection of event candidates for the ZZZ final state. The individual selection criteria are described in Section 5.2.

Table 5.2: Prediction of the Z$\gamma\gamma$, ZZγ and ZZZ event yield in Run 2

Process	MC simulation	Event yields SR
Z$\gamma\gamma$	Sherpa 2.2.4	201.2 ± 4.2
ZZγ	Sherpa 2.2.5	4.97 ± 0.05
ZZZ	Sherpa 2.2.2	0.119 ± 0.002

Leptons originating from a Z boson usually carry higher p_T than 10 GeV. The most reduction of events is caused by the tight identification requirement for the leading electron and the tight isolation criteria for the leading muon. After these selection requirements are applied, the number of signal events expected for the full Run 2 MC dataset is:

$$N_{ZZZ} = 0.119 \pm 0.002 \tag{5.2}$$

The uncertainty comprises the statistical uncertainty only. The resulting event expectation is compared to other triboson production processes involving the Z boson in Run 2. Previous analyses of the $Z\gamma\gamma$ [67] and $ZZ\gamma$ [68] final states are chosen. The resulting event yields of all three processes are listed in Table 5.2. For the $Z\gamma\gamma$ production process, about 201 events are expected. A triboson process with two Z bosons and a photon, $ZZ\gamma$, has an event expectation of 4.97, which is about 1/40 of the event number of the $Z\gamma\gamma$ process. The triple Z boson production in Run 2 predicts an event yield of 0.119 events. Compared to the $ZZ\gamma$ event prediction, the expectation is again reduced by roughly 1/40 of events. The event expectation for each of these triboson processes are reduced by the same ratio, when an additional Z boson is taken into account. Therefore, it can be concluded that the resulting event expectation for the ZZZ production process is consistent with the $Z\gamma\gamma$ and $ZZ\gamma$ event yields. The resulting number of events for the ZZZ final states is very low. In the future, higher energy scales at the LHC will provide new datasets with increased statistics and allow more precise measurements of rare processes, like triboson production processes. In Figure 5.9 the foreseen progress in the high-luminosity (HL) performance at the LHC in shown. The HL-LHC installation is expected to be completed in 2029 [26]. From the completion on, the following two years of operation are assumed to be at near nominal design performance before then entering Long Shutdown 4 (LS4). The instantaneous luminosity (red) is reaching a luminosity of

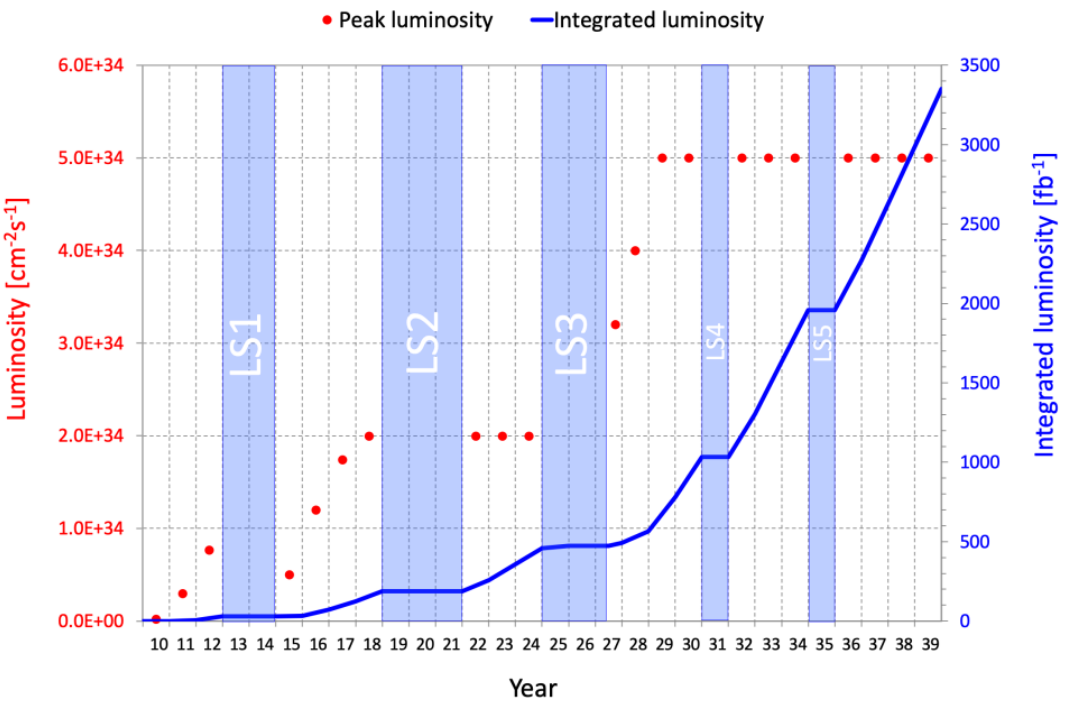

Figure 5.9: Evolution of the HL-LHC performance, where the red is the instantaneous luminosity performance and the blue line is the total integrated luminosity [69].

$5 \times 10^{34}\text{cm}^{-2}\text{s}^{-1}$ and the integrated luminosity (blue) presumably reaches up to a total of $3000\,\text{fb}^{-1}$ by the year 2038 [69]. An estimation can be performed to calculate the expected event number N_{HL} in the high luminosity program for the ZZZ production process. Due to Equation 3.2, the event expectation of a process is directly proportional to the integrated luminosity $\mathcal{L}_{int}$ and the cross-section σ. Using this proportionality, N_{HL} can be calculated as:

$$N_{HL} = N_{Run2} \times \frac{\mathcal{L}_{int}^{HL}}{\mathcal{L}_{int}^{Run2}}. \tag{5.3}$$

By inserting the Run 2 luminosity of $\mathcal{L}_{int}^{Run2} = 140\,\text{fb}^{-1}$, the Run 2 event expectation of $N_{Run2} = 0.119$ for the ZZZ process and the integrated luminosity expectation in Figure 5.9 for the HL-LHC, $\mathcal{L}_{int} = 3000\,\text{fb}^{-1}$, the resulting event expectation for the ZZZ production process in the HL-LHC era is:

$$N_{HL} = 2.6. \tag{5.4}$$

This number is an estimate and is calculated to provide an idea of future prospects in analysing the leptonic final states of the ZZZ production process.

It can be concluded that even with the HL-LHC measurements, the event yields are still low. In order to obtain 10 signal events, an integrated luminosity of about $10000\,\mathrm{fb}^{-1}$ would be necessary. This is far beyond the current HL-LHC expectations. The HL estimation reveals that the purely leptonic signal region of the ZZZ final states do not provide enough statistics to ensure proper analysis. Considering other decays of the Z boson can help investigating the ZZZ production process better for energy scales provided in the near future. Signatures combined of different decay channels could lead to higher results in the signal events than the purely leptonic signal, but possible disadvantages need to be considered. For example, for the hadronic decay mode the signal is more diluted due to higher background contributions. Therefore, an efficient background suppression would be necessary for these signal events.

6 Analysis of the $WW\gamma$ final state

The $WW\gamma$ production process at the LHC was studied with the ATLAS detector at a center-of-mass energy of 8 TeV with corresponding integrated luminosity of $20.2\,\text{fb}^{-1}$ [70]. Currently, a Run 2 analysis for the $WW\gamma$ final states at $\sqrt{s} = 13\,\text{TeV}$ with an integrated luminosity of $\mathcal{L}_{int} = 140\,\text{fb}^{-1}$ is performed by the ATLAS Group [1], which is not officially published yet. The results of this unpublished ATLAS Note are used as a comparison of the results in this thesis. The Run 3 study presented in the following serves as a first look into the $WW\gamma$ production process at $\sqrt{s} = 13.6\,\text{TeV}$. For the comparison to the Run 2 ATLAS Note results, the integrated luminosity of $140\,\text{fb}^{-1}$ of proton-proton collision is used in this Run 3 analysis. In this Chapter, the signal of the $WW\gamma$ final states are defined in Section 6.1 and the corresponding object and event selection is presented in Section 6.2. The resulting event expectation in the signal region is discussed in Section 6.3. In the last Section 6.4, the dominating background processes are outlined and their expected number of events in the signal region is discussed.

6.1 Signal Definition

The $WW\gamma$ process has several signatures as the W boson can decay hadronically, resulting in two jets, or leptonically into a charged lepton and the corresponding lepton neutrino. A disadvantage of a leptonic signal are lower statistics, because the W boson is more than twice as likely to decay into hadrons [71]. The advantage of a leptonic signature is a reduced background contribution compared to the hadronic decay mode. The chosen signature consists of two opposite signed, opposite flavoured (OSOF) leptons ($l = e, \mu$) and a photon: $e^{\pm}\mu^{\mp}\gamma$. The specific composition of this signal is explained in the following. Two same-flavoured leptons in the final state is dominated by $Z\gamma$ processes. Requiring two opposite flavoured leptons in the signal enables to rejected these events. Furthermore, the lepton pair must have opposite charge due to the signature of the quartic gauge boson interaction, displayed in Figure 6.1. Further examples of Feynman diagrams for the $WW\gamma$ production process

are shown in Figure 6.1. In the first diagram, the $WW\gamma$ final state emerges directly from quarks. This production process does not involve interactions between the electroweak force carriers. The following two diagrams are presenting the $WW\gamma$ production involving a triple gauge coupling (TGC) vertex and the last diagram depicts the production process with a quartic gauge coupling (QGC). The triple and quartic gauge boson interaction is mediated by either a Z boson or a photon, which are both electrically neutral. Therefore, both W bosons and the corresponding leptons in the final state carry opposite charge.

The lepton pair of interest consists of two opposite signed, opposite flavoured (OSOF) leptons in addition with the corresponding neutrino and antineutrino: $e^{\pm}\mu^{\mp}\nu\bar{\nu}$. Due to the neutrinos involved, a certain imbalance in the transverse momentum is expected, which is measured as missing transverse energy. The $WW\gamma$ final state also requires a photon, which can emerge from an initial quark as initial state radiation (ISR) or from final state radiation (FSR) from one of the W bosons or its decay products. These arguments result in a signal for the $WW\gamma$ final states of: $e^{\pm}\mu^{\mp}\gamma$. The selection process of this signature is described in the following section.

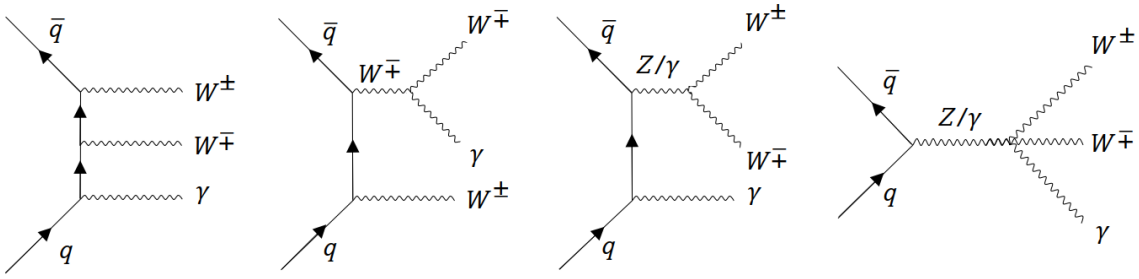

Figure 6.1: Examples of Feynman diagrams for the $WW\gamma$ production process. In the first diagram, the $WW\gamma$ final state emerges directly from quarks. The second and third diagram present the production of the $WW\gamma$ process involving a TGC vertex and the last diagram depicts a process involving QGC.

6.2 Object and Event Selection

The selection procedure aims the identification of interesting objects to the analysis and reducing possible background effects. Similar to the selection of ZZZ final states, an object and event selection is applied for the $WW\gamma$ final states. The selection requirements are strongly oriented on the object and event selection from the ATLAS Note [1]. It is crucial to adapt the same selection in order to ensure a clean comparison between this analysis and analysis in the from the ATLAS Group.

Object Selection

Objects of interest for the $WW\gamma$ final states consist of an electron, muon and a photon. Imposed baseline quality requirements in the object selection are choosing the best lepton and photon candidates. The Run 2 analysis documented in the ATLAS Note uses stringent requirements in the object selection, which are explained in the following.

All events considered further in the selection process must pass the Good Run List to ensure good quality data [59]. A minimum transverse momentum requirement is set to the final state candidates in order to reduce misidentification with other low-p_T objects. Signal electrons, muons and photons have to pass a transverse momentum threshold of $p_T > 20\,\text{GeV}$. Furthermore, the electron and photon candidates must satisfy tight identification and tight isolation criteria [60]. For the muons, medium identification and tight isolation WPs are required [61]. Due to the detector construction, specific pseudorapidity ranges for the reconstruction of the particles must be excluded, as explained in more detail in Section 5.2. Muons are reconstructed within $|\eta| < 2.5$, whereas electrons are required to be reconstructed in the pseudorapidity range of $|\eta| < 2.47$. Photons can be measured up to a pseudorapidity of $|\eta| < 2.37$ and the range of $1.37 < |\eta| < 1.52$ must be excluded for photons as well as for electrons [49]. The limitation on the pseudorapidity range for the photons arise from the required fine granularity of the first EM calorimeter layer. Within the mentioned acceptance region, the high granularity provides discrimination between single-photon showers and two overlapping showers from neutral hadron decays on an event-by-event basis [72]. For jets, a higher pseudorapidity region is covered by the hadronic forward calorimeter and these objects are measured for $|\eta| < 4.4$ [62]. The signal lepton candidates are required to originate from the primary vertex. There-

fore, pile-up contributions need to be reduced. As already explained in Section 5.2, requirements on the transverse (d_0) and longitudinal (z_0) impact parameters of tracks are placed. Electron and muon tracks must satisfy $|\Delta z_0 \sin\theta| < 0.5$ mm for the longitudinal impact parameter. The transverse impact parameter d_0, is divided by its estimated uncertainty (σ_{d_0}) and must fulfil $|\Delta d_0/\sigma_{d_0}| < 5.0$ and < 3.0 for electrons and muons, respectively [64].

The pile-up contribution for jets must also be suppressed and therefore jets need to pass the jet vertex tagger (JVT) to separate hard-scatter jets from pile-up jets. This is done by an algorithm that uses information from the calorimeter, the ID and the tracks of the jets. It is required, that tracks associated with the primary vertex make up a significant fraction of the summed track p_T of the jets [64]. To ensure proper separation of the signal objects in the $\eta - \phi$ space and to avoid misidentification, it is crucial to assign the right particles in the reconstruction process. Therefore, an overlap removal is performed on the lepton and photon candidates. Electrons are removed at a distance to muons of $\Delta R(e, \mu) > 0.1$. Photons tracked in a cone of $\Delta R(\gamma, l) < 0.4$ around an electron or muon are excluded. Jets are removed, if they are reconstructed within $\Delta R(j, e) < 0.2$ of an electron and $\Delta R(j, e) < 0.4$ of a photon. In Table 6.1 the full object selection requirements are listed along with the event section, which is presented in the succeeding.

Event Selection

To select the signal events, additional requirements are placed in the event selection. First, the selection requires at least two leptons, where one electron and one muon must be present and have opposite charge. For the lepton with the higher transverse momentum, the leading lepton, a transverse momentum of greater than 27 GeV must be satisfied. This p_T-requirement ensures efficient working of the single-lepton triggers, which select events in data with at least one high-p_T lepton. Furthermore, at least one photon is required, which meets the requirements mentioned in the object selection. Due to neutrinos resulting from the W decay, the $WW\gamma$ final states carry missing transverse momentum. The events have to fulfil $E_T^{miss} > 20$ GeV. The selection process of the $WW\gamma$ final states must also consider other processes that could mimic the signal. Especially processes with higher cross-section that can dilute the signal, must be suppressed in the event selection. A process that could mimic the event signature of $e^{\pm}\mu^{\mp}\gamma$ is the $t\bar{t}\gamma$ production process. The top quark decays into

a W boson and a b quark with the highest branching ratio. To reduce contributions from this final state, a veto is set on events that contain a b-jet passing a 85 % efficiency working point. The leptonic decay of the ZW production process has to be considered as well. The decay mode $ZW \to e^{\pm}e^{\mp}\mu^{\pm}\nu_{\mu}$ can produce the signal, if the electron with the same sign as the muon is misidentified as a photon. To sort out these events, the mass of the electron and photon pair must satisfy $|m(e,\gamma) - m_Z| > 5\,\text{GeV}$, where $m_Z = 90\,\text{GeV}$.

Table 6.1: Object and event selection requirements of the $WW\gamma$ signal.

	Requirements
Leptons	Leading lepton: $p_T > 27\,\text{GeV}$
	Subleading lepton: $p_T > 20\,\text{GeV}$
Electrons	Tight ID
	Tight isolation
	$\lvert\eta\rvert < 2.47$, excluded $1.37 < \lvert\eta\rvert < 1.52$
	$\lvert\Delta d_0/\sigma_{d_0}\rvert < 5.0$, $\lvert\Delta z_0 \sin\theta\rvert < 0.5\text{mm}$
Muons	Medium ID
	Tight isolation
	$\lvert\eta\rvert < 2.5$
	$\lvert\Delta d_0/\sigma_{d_0}\rvert < 3.0$, $\lvert\Delta z_0 \sin\theta\rvert < 0.5\text{mm}$
Photons	Tight ID
	Tight isolation
	$p_T > 20\,\text{GeV}$
	$\lvert\eta\rvert < 2.37$, excluded $1.37 < \lvert\eta\rvert < 1.52$
Multiplicity	at least 2 OFOS leptons
	at least 1 electron and 1 muon
	at least one photon
Overlap removal	$\Delta R(e,\mu) > 0.2$, $\Delta R(j,e) < 0.2$,
	$\Delta R(\gamma, l) < 0.4$
Missing E_T	$E_T^{miss} > 20\,\text{GeV}$
b-Jet	N(b-jets) = 0 with 85 % b-tag working point
Mass cut	$\lvert m(e,\gamma) - m_Z\rvert > 5$

6.3 Signal extraction

The resulting event yields in the $WW\gamma$ signal region on Run 3 energies are presented in this Section. The results are compared with an ongoing Run 2 analysis in an ATLAS Note. For further comparison and investigation, the $WW\gamma$ Run 2 MC sample used in the ATLAS Group analysis, is included and analysed. The event expectations presented in the succeeding are obtained for proton-proton collisions with an integrated luminosity of $\mathcal{L} = 140\,\mathrm{fb}^{-1}$.

The results in the $e^{\pm}\mu^{\mp}\gamma$ signal region are summarized in Table 6.2. The first and second event yields are respectively the Run 3 and Run 2 results, generated in this study. The last event number is extracted from the ATLAS Note and is marked with "*". The effort in the analysis process is to narrow down deviations from the ATLAS Group analysis as far as possible in order to provide a solid base for the Run 3 study. To examine for differences, a cross-check is performed by applying the event selection process of this thesis on the same Run 2 MC signal sample from the ATLAS Note. Excluding major deviations in the results for the same MC sample ensures an assimilated selection process. All MC samples used in this study are summarized in Chapter 2, Table 2.4. The officially produced Run 2 MC sample for the $WW\gamma$ final states is generated in Sherpa 2.2.11 with on- and off-shell contributions and an accuracy of NLO QCD precision. In Table 6.2, the Run 2 event expectation of this study are 313.5 events, whereas the ATLAS study [1] results an event expecation of 239.0. The results differ by 74.5 events, whereby the result generated in this thesis is about 30 % higher. Although, the selection of the $WW\gamma$ final states is strongly oriented on the selection of the ATLAS Note, possible deviations may be missed. Also, the generation process of the n-tuples can differ for both samples, where differences in the pre-selections may be present. To localize discrepancies, various cross-checks are performed. Every selection requirement in this study is cross-checked with all presented requirements in the ATLAS Note to ensure the selection in both studies are in agreement. To compare the impact of each selection variable on the event expectation, a cut-flow diagram from the ATLAS Note was searched for and requested, but unfortunately a cut-flow diagram was not available. Comparing both cut-flow diagrams could have helped localizing problems and deviations in the selection process further and possibly reveal sources of discrepancies. Thus, the effort of equalizing both selection processes reached a limit.

Table 6.2: Prediction of the event yields in the $e^{\pm}\mu^{\mp}\gamma$ signal region for a Run 3 MC sample and a Run 2 sample. As a reference value, the event expectation from the ATLAS Note [1] is included and is marked with "*".

$WW\gamma$ Process	MC simulation	Event yields SR
Run 3	MadGraph 2.9.9	142.0 ± 2.2
Run 2	Sherpa 2.2.11	313.5 ± 10.0
Run 2*	Sherpa 2.2.11	239.0 ± 10.7

Regarding various performed cross-checks, the limited ability of assimilating both selections and given the statistical uncertainties, the Run 2 result generated in this study is considered to be in acceptable consistency with the result from the ATLAS Note.

As described already in Chapter 2, an officially produced $WW\gamma$ sample for Run 3 energies was not available at the time this analysis was performed. Therefore, the signal sample is self-produced in MadGraph 2.9.9 for the purpose of this study. Since, same integrated luminosity is used for the analysis of the Run 3 and Run 2 MC dataset, the event expectation on Run 3 energies can be estimated from the Run 2 result. The Run 3 center of mass energy of $\sqrt{s} = 13.6\,\text{TeV}$ is about 5 % higher than the Run 2 energy of $\sqrt{s} = 13\,\text{TeV}$. Hence, the expected event yields should also increase 5 % for the Run 3 study. Taking the reference value of the ATLAS Note of 239 events, this would yield an event expectation of $N = 250$ events. The resulting event expectation in Table 6.2 generated in this thesis for the Run 3 analysis is 142 events, which is only about 57 % of the expected 250 events. Unlike the discussion of the Run 2 event expectations, small deviations in the selection process can not justify such a large difference in the results. Critical malfunctions and bugs in the implementation of the event selection and the generation process of the MC sample must be investigated. In order to gain more insight, the most significant cross-checks are discussed in the proceeding.

First, to verify the Run 3 MC sample is generated properly and no inconsistencies within the dataset occur, various examinations are performed and compared to the

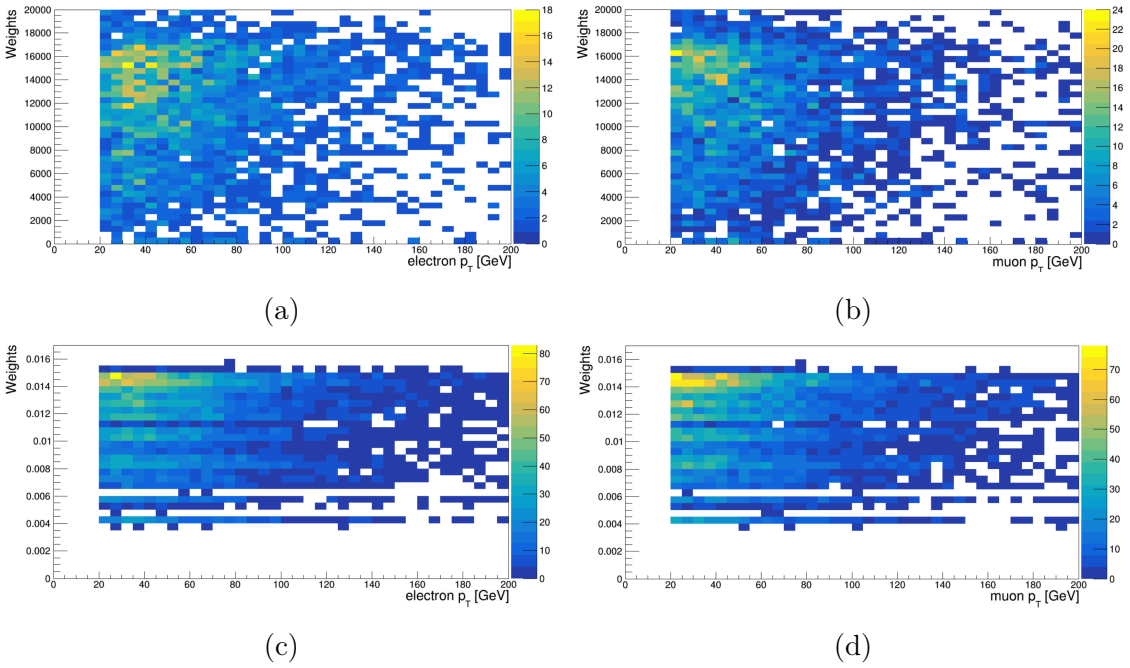

Figure 6.2: Distribution of the weights against the transverse momentum variable of the Run 2 sample in (a) electron-p_T and (b) muon-p_T and of the Run 3 sample in (c) electron-p_T and (d) muon-p_T.

officially produced Run 2 signal sample. An investigation for probable irregularities in the weights is performed in order to examine the generation process of the n-tuples. Abnormalities in the weight distributions can hint into deeper problems of the MC sample. The weights are plotted against kinematic variables in two dimensional plots for the Run 2 and Run 3 MC samples, shown in Figure 6.2. The distributions in (a) and (b) show the weight distributions of the Run 2 sample in dependence of the electron-p_T and muon-p_T, respectively, whereas the distributions in (c) and (d) depicts for the Run 3 sample the weights depending of the electron-p_T and muon-p_T, respectively. The two dimensional distributions result an evenly and symmetrically distribution for both samples. The weights do not reveal any fluctuation or any abnormal pattern throughout the p_T values. It can be validated that the weights are properly set in the MC samples.

Main differences between the Run 3 and Run 2 MC samples are the different MC generators and the generation process itself, since the Run 3 sample is not officially produced by the ATLAS Collaboration. These differences may cause deviating re-

sults. To investigate the generation process of the Run 3 signal sample, different stages of the MC simulation are examined separately and the results are evaluated. As explained in Chapter 2, the simulation process of a MC sample is divided into two different stages, at truth level and reconstruction (reco) level. The pre-selection process, described in Section 6.2, places restrictions on the events directly on reco level and is not performed on truth level. Thus, interesting events to the signal are selected only on reco level and exclusively those selected events are stored with their associated truth information. Due to this specific pre-selection process, the events on reco level are already affected by the selection criteria, whereas on truth level the events are stored without experiencing any selection requirements. Investigating the signal MC samples separately on truth level and reco level, provides insights into potential inconsistencies along the generation process.

In the succeeding, the event yields on truth and reco level are generated separately and compared to each other. An additional separation is applied for the baseline selection (BL) and the event selection (ES) requirements. To be able to compare the results on truth level and reco level, the identification and isolation working points are excluded in the event selection, since these efficiencies are only present in the reconstruction process. Thus, the event expectations in this comparison generated with the selection requirements described in Section 6.2, but without the identification and isolation working points. This investigation ensures that the sample is consistent within. Any abnormalities in the results would hint to a problem in the generated sample. The results for the Run 3 MC dataset are listed in Table 6.3.

Table 6.3: Event expectations in the $e^{\pm}\mu^{\mp}\gamma$ signal region of the Run 3 MC sample for $WW\gamma$ final states. The event yields are calculated separately for the truth and reco level. The results are shown for the baseline selection (BL) requirements and the event selection (ES).

	BL Run 3	ES Run 3	Factor
Truth	228.2	182.6	1.2
Reco	229.6	211.0	1.1
Factor	1.0	1.2	-

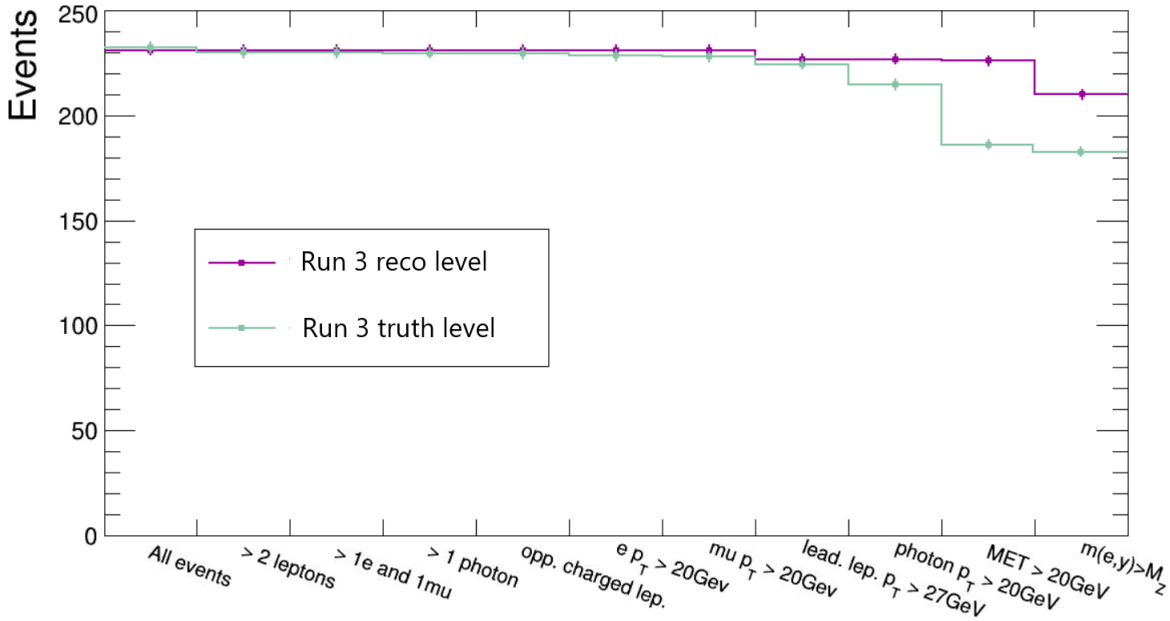

Figure 6.3: The cut-flow diagrams shown on truth level (green) and on reco level (purple) for the Run 3 signal sample.

Regarding the BL, the resulting event expectations on truth and reco level are in agreement with each other, where 228.2 events are selected on truth and 229.6 events on reco level. After the ES is applied, the consistency between both simulation level deteriorate slightly. The number of expected events are 182.6 and 211.0 events on truth and reco level, respectively. The event yields show a small deviation by a factor of 1.2. This is caused by the specific procedure of the pre-selection, explained above, where the pre-selection is directly applied on the reco level event. The events on truth level do not experience pre-selection criteria and are therefore more affected by the event selection. The difference in the event yields between the truth and reco level is also shown in the comparison of the cut-flow diagrams in Figure 6.3. The purple and green distributions are the reco and truth level cut-flow diagram, respectively. As expected, the first six selection requirements do not impact the event number on reco level but do reduce events on truth level. A reduction on truth level compared to the reco level, appears for the lepton- and photon-p_T requirements of $p_T > 20\,\text{GeV}$ and MET $>$ 20GeV, since these selection requirements appear exclusively in the event selection.

Table 6.4: Comparison between the Run 3 and Run 2 samples for $WW\gamma$ final states. The event expectations in the $e^{\pm}\mu^{\mp}\gamma$ signal region are calculated separately on truth and reco level for the BL and ES for each sample. Additionally, the factors of deviation are shown and compared between both samples.

	Run 3			**Run 2**		
	BL Run 3	ES Run 3	Factor	BL Run 2	ES Run 2	Factor
Truth	228.2	182.6	1.2	469.6	399.4	1.2
Reco	229.6	211.0	1.1	472.3	441.7	1.1
Factor	1.0	1.2	-	1.0	1.1	-

The consistency of the Run 3 signal sample can be further solidified, by investigating the officially produced Run 2 $WW\gamma$ signal sample and comparing the results. In Table 6.4, the results for both samples are listed. The Run 2 sample shows similar outcomes as the Run 3 sample. For the BL, both samples show the same agreement in event expectations between the truth and reco level. For the ES, the Run 2 sample reveals a small difference between the truth and reco level event yields. This is again due to the pre-selection process explained above. The deviation factors are similar on both samples. Thus, the comparison with the Run 2 sample confirms the assumption of a consistent Run 3 signal sample.

Another cross-check between the Run 2 and Run 3 sample is performed in Table 6.5. Here, the event expectations between both samples are compared within the BL and ES. Compared to the Run 2 sample, the Run 3 sample shows already significantly lower results after the BL is performed. The difference in the event yields is by a factor of 2.05 after the BL. The deviation increases after the ES is applied and reveals a deviation by a factor of 2.2 on truth level and 2.1 on reco level. This observation shows that the event expectation for the Run 3 sample is effected more by the selection requirements of the ES. Although, this observation does not necessarily point out an error in the Run 3 sample, it can hint to an underlying effect concerning the sample, which may provides deeper understanding for the deviating results of both MC samples. To examine this observation further, the cut-flow diagrams of both

Table 6.5: Comparison between the Run 3 and Run 2 event yields in the $e^{\pm}\mu^{\mp}\gamma$ signal region for the BL and ES separately. The results are shown on truth and reco level and the factors of deviation are listed.

	BL			**ES**		
	Run 3	Run 2	Factor	Run 3	Run 2	Factor
Truth	228.2	469.6	2.05	182.6	399.4	2.2
Reco	229.6	472.3	2.05	211.0	441.7	2.1

samples are compared. These diagrams reveal the effects of the specific selection requirements on each sample. The cut-flow diagrams after the full ES on reco level are compared in Figure 6.4, whereby the red and blue distributions are the Run 3 and Run 2 samples, respectively. For a clean comparison, both histograms are normalized to one and the displayed event loss corresponds to a proportional value. The comparison reveals that different criteria have different impact on each sample. For example, the Run 3 sample looses more events after the requirement for the leading lepton of $p_T > 27\,\text{GeV}$. Therefore, the transverse momentum distributions of the leading lepton is investigated further. In Figure 6.5, the distributions for both samples are normalized to one and compared, where the red distribution is again the Run 3 sample and blue is the Run 2 sample. The leading lepton p_T distributions are shown on truth level and after the BL is applied, to ensure that effects from the detector simulation do not affect this deviation. The comparison displays different shaped distributions between both samples. The entries at low-p_T values are consequently higher for the Run 3 sample. For higher values, both distributions show better agreement. Such a deviation in shape is found to be present in all kinematic distributions between both samples. This observation is made on truth level, before the ES is applied. Thus, the difference in shape is not caused by differences in the detector simulation and particle reconstruction of the two MC generators, but is already present on particle level.

The cut-flow diagrams show no reduction for the identification and isolation WP requirements of the electron and muon. These WPs are already selected in the object selection and are part of the BL. The WPs for the photon on the other hand, are selected in the ES. The requirements for the photon tight identification and tight

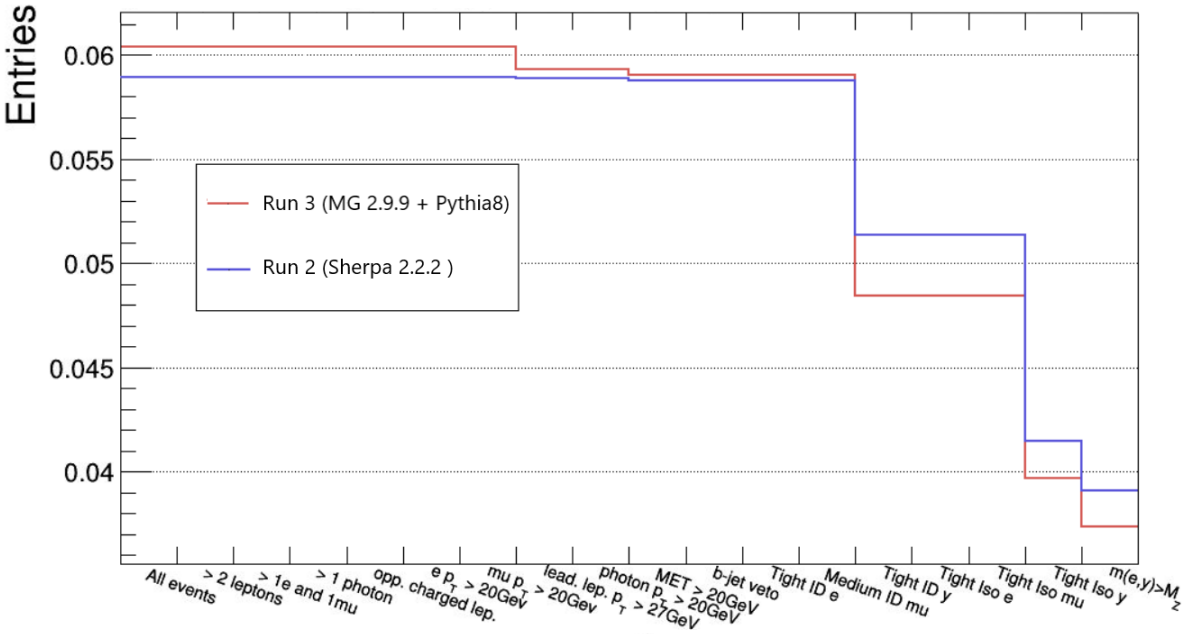

Figure 6.4: The cut-flow diagrams of the Run 3 sample (red) and the Run 2 sample (blue) with the selection criteria described in Section 6.2. The distributions are shown on reco level and are normalized to one for comparison.

isolation causing a large event loss in both samples. The Run 3 sample reveals a greater proportional loss than the Run 2 sample. The photon tight identification criteria reduces the event number for the Run 3 sample by 19 %, whereas the Run 2 event yields are reduced by only 13 %. To exclude any bugs in the implementation of the tight identification requirement in the ES, the histogram from the n-tuples, shown in Figure 6.6, is investigated. All entries greater than one fulfil the tight requirement. The entries smaller than one are excluded in the selection process and correspond to 19 % of the entries. This is equal to the event loss in the cut-flow diagram. In the same manner, the photon tight identification for the Run 2 signal sample is cross-checked and no inconsistencies are found. This investigation is also performed for the photon tight isolation requirement in both samples. After these cross-checks, major mistakes in the implementation of the ES appear to be unlikely. However, the observation of different shaped kinematic distribution between both samples is revealed. Different shaped kinematic distributions can occur due to the different MC generators used for the production of the Run 3 and Run 2 signal samples. Even slight differences can cause significant deviations in the resulting event yields. To examine the kinematic distributions of both samples further, the lepton-

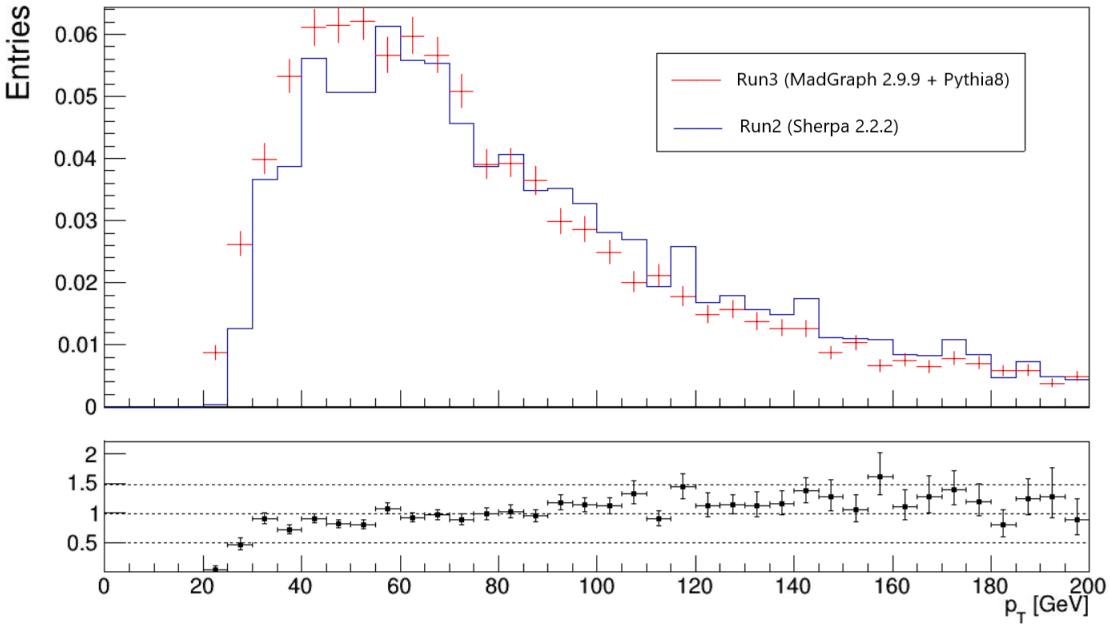

Figure 6.5: The transverse momentum distribution of the leading lepton from the Run 3 sample (red) and the Run 2 sample (blue). The distributions are shown on truth level with BL and are normalized to one for comparison.

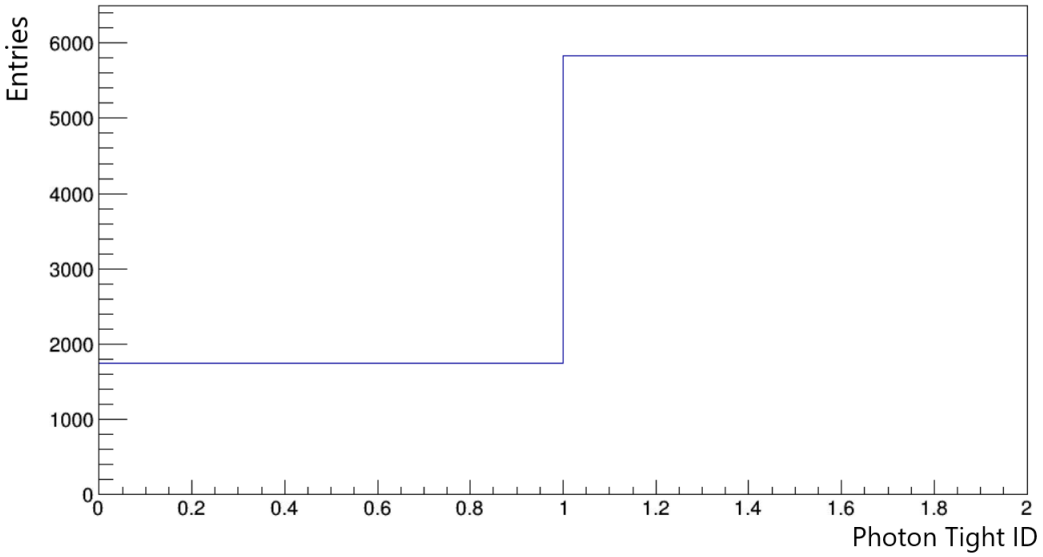

Figure 6.6: Distribution of the photon tight identification from the n-tuples of the Run 3 sample.

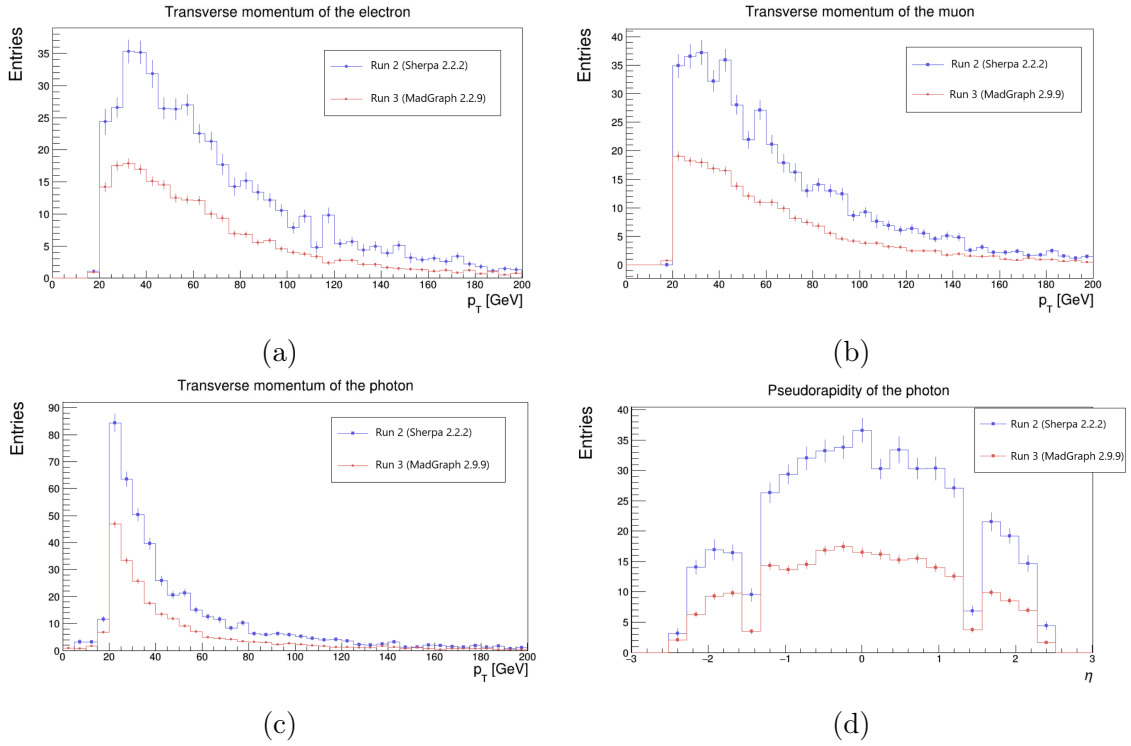

Figure 6.7: Kinematic distributions on truth level of the Run 2 sample (blue) and Run 3 sample (red) after the BL, where (a), (b) and (c) are the transverse momentum distribution for electron, muon and photon, respectively, and (d) shows the photon pseudorapidity distribution.

and photon-p_T distributions along with the photon pseudorapidity distribution for the Run 3 (red) and Run 2 (blue) samples are presented in Figure 6.7. The presented distributions are generated on truth level after the BL is performed. As explained before, the events on truth level do not experience any selection requirements and therefore provide a clean opportunity to compare the shapes.

The comparison shows that the Run 3 distributions are consequently shifted towards lower entries compared to the Run 2 distributions. These shifted distributions are further examined in the following. Regarding again the event expectations for both samples in Table 6.5. On truth level at the BL, the Run 2 event expectation is larger by a factor of 2.05. To examine, if this factor is a global scaling issue in the Run 3 sample, the kinematic distributions are investigated further. All distributions of the Run 3 sample on truth level are scaled with the factor of 2.05. The resulting scaled kinematic distributions of the lepton and photon-p_T and the photon pseudorapidity

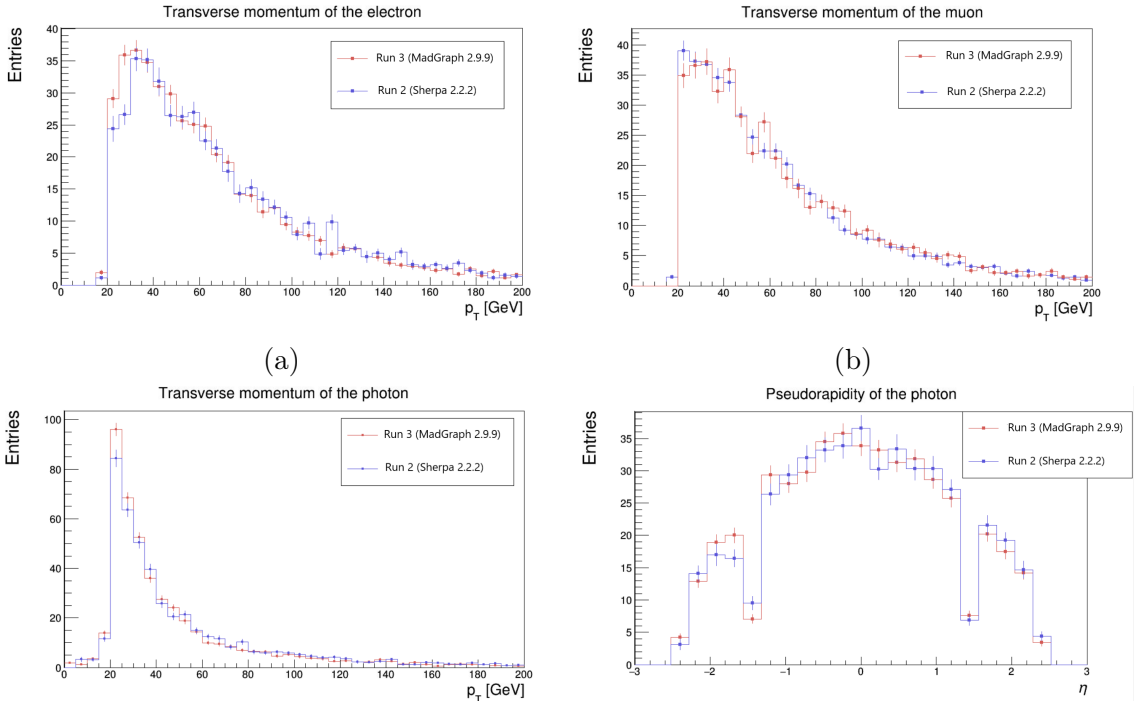

Figure 6.8: Kinematic distributions on truth level of the Run 2 sample (blue) and Run 3 sample (red) after the BL, that are scaled by a factor of 2.05 and compared to the unscaled Run 2 sample distributions (blue), where (a), (b) and (c) are the transverse momentum distribution for electron, muon and photon, respectively. Distribution (d) shows the photon pseudorapidity.

are compared to the distributions of the Run 2 sample in Figure 6.8. The distributions are showing better alignment after the scaling factor is applied on the Run 3 distributions. This finding hints that the problem is a globally issue in the Run 3 sample and is not concerning one specific selection requirement.

After several cross-checks, the assumption arise that the generation process of the Run 3 MC sample is run properly and the sample is consistent within. Especially the comparison with the officially produced Run 2 sample ensures the consistency of the Run 3 sample. Serious malfunctions in the implementation of the selection process are investigated and identified problems are excluded. Deviations in the shape of the kinematic distributions between both signal samples are observed and their impact on the event yields are discussed.

The observed differences between the results of the Run 2 and Run 3 signal samples can have several roots. The Run 3 sample is self-generated and unidentified mistakes in the generation process can be present. The implementation of the physical process can be inaccurate by setting up incorrect configurations or initial requirements. Additionally, during the simulation process issues in the detector simulation and reconstruction of the particles can lead to invalid results. Statistic fluctuations can play a role, but the generated datasets are large and the fluctuations should be negligible. The samples compared in this Section are generated with different MC generators, MadGraph and Sherpa. Comparing MC samples from different generators could have an effect on this study and are discussed further in Section 6.4.3. Furthermore, the problem can be a systematic issue concerning the MadGraph generator. This needs further investigation, but is beyond the scope of this thesis.

6.4 Background Estimation

When selecting the signal events of the $WW\gamma$ production process, background processes have to be considered. The goal is to reduce the background contribution as much as possible while keeping the signal events in the selection process, but this is only possible to some extent. An estimation of the largest background processes is performed in this Chapter. First, the $t\bar{t}\gamma$ process is described and the expected event yields in the signal region is presented. Afterwards, the $Z\gamma$ final states are discussed and the expected number of events in the signal region is shown.

6.4.1 $t\bar{t}\gamma$ Background

Top quark pairs are mainly produced in the QCD process $q\bar{q} \rightarrow t\bar{t}$ in proton-proton collisions. The largest decay width of the top quark is the decay into a W boson and a b-quark, $t \rightarrow bW^+$ [66]. The production of the photon in the $t\bar{t}\gamma$ final states can be distinguished into two different processes. The photon can either radiate from one of the decay products of the top quark or radiate directly from the hard-scattering. Thus, the $t\bar{t}\gamma$ final states are divided into two separate production processes: $q\bar{q} \rightarrow t\bar{t}\gamma$ (*production*) and $t \rightarrow bW\gamma$ (*decay*). Figure 6.9 shows representative Feynman diagrams for the $t\bar{t}\gamma$ process production. The first diagram presents the *production* process. where the photon radiates directly from one of the initial quarks. The second diagrams shows the *decay* process, where the photon is emitted from a decay product of the top quark.

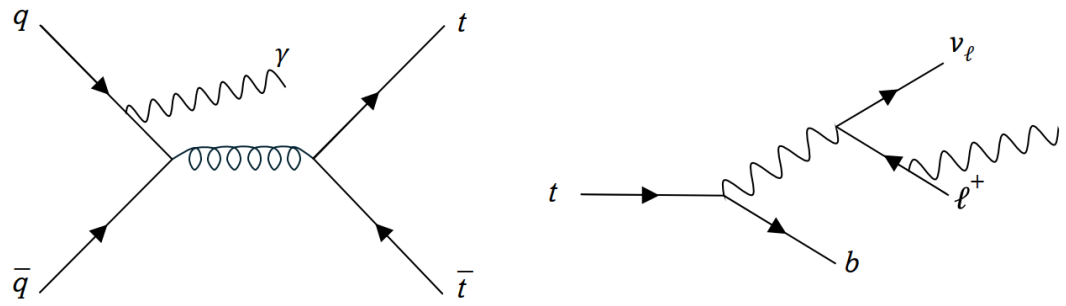

Figure 6.9: Feynman diagrams for the $t\bar{t}\gamma$ production process in leading order (LO). The first diagram shows photon radiation from the hard-interaction and the second diagram illustrates the photon resulting from one of the decay products of the top quark.

If both of the W bosons decay leptonically, the $t\bar{t}\gamma$ process can mimic the $e^{\pm}\mu^{\mp}\gamma$-signal without the need of non-prompt leptons: $t\bar{t}\gamma \rightarrow W^+bW^-\bar{b}\gamma \rightarrow e^+\mu^-\nu\bar{\nu}b\bar{b}\gamma$. Here, the main difference to the $WW\gamma$ final states is the existence of b-jets. Besides the direct decay from the W bosons, the signal leptons can also originate as indirect decay products of the τ-leptons in the process: $t \rightarrow Wb \rightarrow \tau\nu b$. In order to investigate the contribution of signal leptons from the τ-lepton decay, the origin of the leptons are observed. This is performed on particle level, because the particle origin information is saved in the truth information. The results are presented in Figure 6.10, after the full event selection is performed on truth level. The histogram (a) shows the electron origin and (b) the muon origin. The histograms reveal that the selected signal leptons solely originate directly from the top quark. Electrons and muons from the τ-lepton decay are included in the MC sample, but these signal leptons possibly gets rejected in the event selection process. The signal lepton candidates originated from the τ-decay, carry less energy than the leptons decaying directly from the top quarks and therefore get rejected due to the transverse momentum requirements. At the time this study was performed, an officially produced $t\bar{t}\gamma$ sample for Run 3 energies was not available. Therefore, the MC sample is self-produced in MadGraph 2.2.9., where the simulation is strongly oriented on the ATLAS Note [1] to enable a sufficient comparison. The study of the $t\bar{t}\gamma$ background process is done by including two different MC samples: $t\bar{t}\gamma$ *decay* and $t\bar{t}\gamma$ *production*. The $t\bar{t}\gamma$ *production* sample is generated at NLO QCD precision. The $t\bar{t}\gamma$ *decay* sample is generated

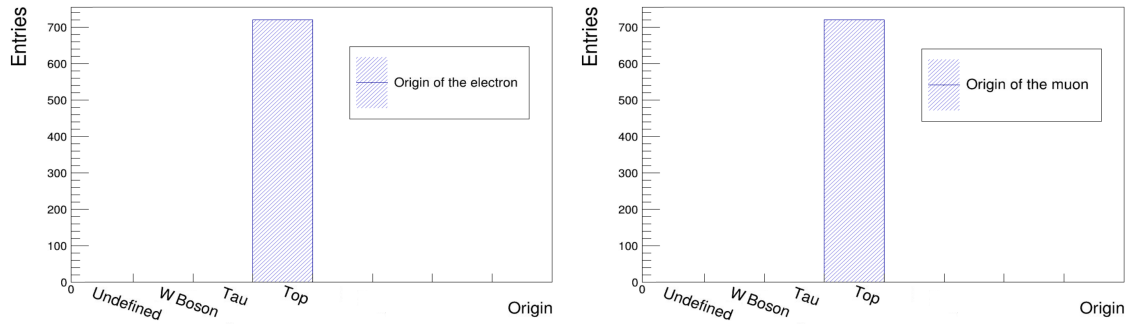

(a) (b)

Figure 6.10: Particle origin of the selected signal leptons from the truth information. Histogram (a) shows the origin of the signal electron and (b) of the signal muon.

Table 6.6: Resulting event expectations in the $e^{\pm}\mu^{\mp}\gamma$ signal region for the $t\bar{t}\gamma$ production process. The result for Run 3 MC sample is generated in this study and the result from the Run 2 MC sample is included from an ongoing ATLAS analysis [1] as a reference value and is marked with "*".

$WW\gamma$ Process	MC simulation	Event yields SR
Run 3	MadGraph 2.9.9	561.7 ± 63.5
Run 2*	MadGraph 2.7.3	411.5 ± 36.3

with a $t\bar{t}$ production at LO followed by the decay of top quarks at LO, where either of the top-quarks radiates a photon. Both MC samples are included in the estimation of the event expectation. The expected number of events for the $t\bar{t}\gamma$ background in the $e^{\pm}\mu^{\mp}\gamma$ signal region is presented in Table 6.6. The event yield from the ATLAS Note is also included and serves as reference value. The Run 3 MC sample result an event expectation of 561.7 events, whereas the Run 2 study from the ATLAS Note present 411.5 expected events [1]. The result in this study is 36 % higher than the event yield in the ATLAS Note. Several cross-checks were performed in order to exclude any major malfunctions in the $t\bar{t}\gamma$ MC dataset and in the event selection. All kinematic distributions are investigated and no inconsistencies are found. A hint towards the underlying issue could be the examination described in Section 6.3, where the event selection is performed on the same Run 2 signal MC sample from the ATLAS Note.

This observation revealed that the event yield generated in this study is 30 % higher than the ATLAS Note. Deviations in the selection process between both studies are assumed to be present, which could also affect the result of the $t\bar{t}\gamma$ production process. To further investigate this assumption, more detailed studies are needed in order to obtain an assimilated selection processes between both analyses and ensure a clean comparison.

6.4.2 $Z\gamma$ Background

The leptonic decay of the Z boson consist of a same-flavour, opposite-sign (SFOS) lepton pair, i.e. $e^+e^-, \mu^+\mu^-$ or $\tau^+\tau^-$. Representative Feynman diagrams of the $Z\gamma$ final states are shown in Figure 6.11. In the first diagram, the photon is produced directly in the hard-interaction, where as in the second diagram the photon is radiated from one of the decay products of the Z boson. In order to mimic the $e^{\pm}\mu^{\mp}\gamma$ signal, one misidentified lepton is required. The only decay mode that enters the signal region without the need of a misidentified lepton is the Z boson decay into a pair of two τ-leptons. Then the τ-leptons decay leptonically in the decay channel: $\tau \rightarrow l\nu_l\nu_\tau$, SFOS electron-muon pairs can be created. The neutrinos in this decay mode leaves an imbalance in the transverse energy observable. Hence, this signature is very similar to the the $WW\gamma$ signal events. It is expected that the majority of the selected events in the signal region originate from the τ-channel. Events from the Z boson decay into two electrons or two muons are assumed to be suppressed. To investigate this assumption, the three different decay channels are studied sepa-

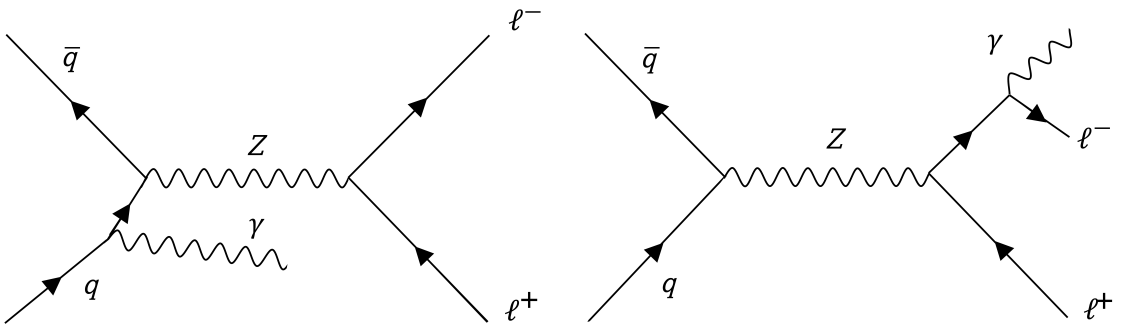

Figure 6.11: Example Feynman diagrams of the $Z\gamma$ production in the leptonic decay channel, where the first diagram shows the photon production in ISR and the second diagram depicts the photon from FSR of a decay product of the Z boson.

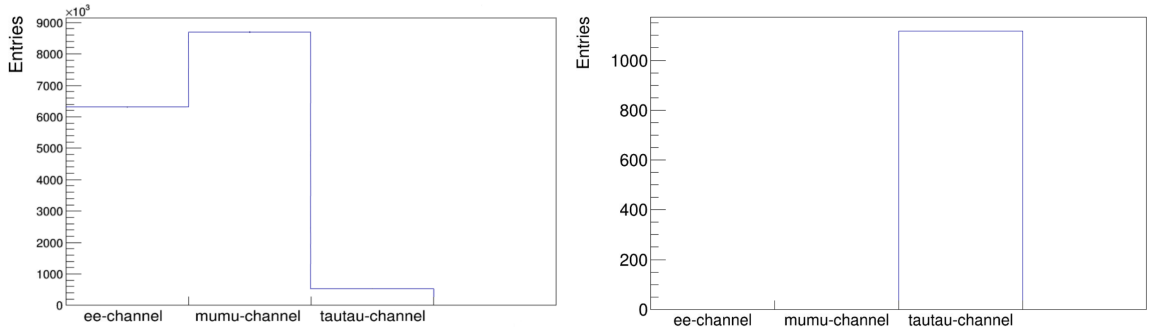

(a) (b)

Figure 6.12: Event candidates in the $WW\gamma$ signal region in the different decay modes of the $Z\gamma$ final states shown on truth level, where (a) presents before and (b) after the ES is applied.

Table 6.7: Resulting event expectations in the $e^{\pm}\mu^{\mp}\gamma$ signal region for the $Z\gamma$ production process. The result for the Run 3 MC sample is generated in this study and the result from the Run 2 MC sample is included from the ATLAS Note [1] as a reference value and is marked with "*".

$WW\gamma$ Process	MC simulation	Event yields SR
Run 3	MadGraph 2.9.9	210.4 ± 30.1
Run 2*	Sherpa 2.2.11	122.5 ± 10.7

rately for the $Z\gamma$ production process. In Figure 6.12, the different decay modes are shown on truth level before and after the ES is applied in (a) and (b), respectively. In the first histogram (a), selected events from the electron- and muon-channels are present with larger contribution than events from the tau-channel. After the ES is applied for the $e^{\pm}\mu^{\mp}\gamma$ signal, only events from the tau-channel satisfy the selection requirements. As expected, the decay modes that require a misidentified lepton in the signal region are suppressed and excluded in the selection process.

The Run 3 MC sample for the $Z\gamma$ production process is self-generated with MadGraph 2.9.9 for the purpose of this study. In the ATLAS Note, a Run 2 MC sample generated with the Sherpa 2.2.11 generator is used. Both samples are simulated at NLO QCD precision with on and off-shell Z boson contributions.The resulting event expectation for the $Z\gamma$ final states are shown in Table 6.7. In this study, an

event yield of $N = 210.4$ is estimated, which is about 72 % larger than the event expectation of $N = 122.5$ from the ATLAS Note [1]. Different cross-checks are performed to ensure a proper selection process and exclude major inconsistencies in the MC sample. As discussed for the $t\bar{t}\gamma$ background analysis, the reason for the large deviation in the event yields is assumed to result from unidentified differences in the selection process between this study and the ATLAS Note.

6.4.3 Overview

Table 6.8: Overview of the resulting event yields for the $WW\gamma$ analysis in the $e^{\pm}\mu^{\mp}\gamma$ signal region. The Run 3 results are generated in this thesis and the Run 2 results are extracted from the ATLAS Note [1].

	Process	Run 3	Run 2	Deviation
Signal	$WW\gamma$	142.0 ± 2.2	239.0 ± 10.7	9σ
Background	$tt\gamma$	561.7 ± 63.5	411.5 ± 36.3	2σ
	$Z\gamma$	210.4 ± 30.1	122.5 ± 10.7	3σ

The event yields for the $WW\gamma$ analysis are summarized in Table 6.8. The Run 3 results are generated in this thesis, whereas the Run 2 results are extracted from the ATLAS Note [1] for comparison. The deviation in the results between both analyses are shown. The event expectations in the $WW\gamma$ final states have the largest disagreement with 9σ. The background processes show less deviation, where the results for the $tt\gamma$ process differs by 2σ and for the $Z\gamma$ process by 3σ. Thus, the largest agreement are observed for the $tt\gamma$ final states. The MC samples for this background process in both analyses are generated with the same MC generator, MadGraph. This is not the case for the $WW\gamma$ and $Z\gamma$ final states. For these production processes, the ATLAS analysis uses MC samples produced in Sherpa, whereas this study uses samples produced in MadGraph, as shown in Table 2.4.

Therefore, comparing the deviations in Table 6.8 reveals that the least difference is present for MC samples with the same MC generator. Different MC generators show larger differences in the event expectations. This observation could be a hint on effects of different MC generators on the analysis of the $WW\gamma$ production process.

MC generators use different algorithms to calculate the matrix element, the cross-section or the parton-showers of a process. QCD- and EWK-corrections can deviate, which can lead to differences in the kinematic distributions. Other analyses, investigating and comparing the predictions of different MC generators on boson and multi-boson states, also have discovered differentiating results [73,74]. To understand the deviating results between this study and the ATLAS study deeper, differences for the $WW\gamma$ production process between the SHERPA and MADGRAPH simulations need to be investigated further, but this extends the scope of this thesis.

7 Conclusion

The studies presented in this thesis are the first study of ZZZ final states for the Run 2 and of $WW\gamma$ final states for the Run 3 of the ATLAS detector. Studying these processes is an important contribution to probe the electroweak sector of the SM and its predictions for gauge boson self-interactions. Contributions of anomalous triple and quartic gauge couplings involving weak gauge bosons provides the possibility to test theories beyond the SM.

The large quantity of data recorded by the ATLAS detector during the Run 2 with an integrated luminosity of $\mathcal{L}_{int} = 140$ fb^{-1} and a centre-of-mass energy of $\sqrt{s} = 13$ TeV allows a first glimpse into the rare ZZZ production process. Only the leptonic decays of the three Z bosons are considered as signature, which constructs a signal of three OSSF lepton pairs: $3(l^{\pm}l^{\mp})$. The expected number of signal events obtained in this study for Run 2 is $N = 0.119 \pm 0.002$. An estimation for the HL operation at the LHC for $\mathcal{L}_{int} = 3000$ fb^{-1} results in an event expectation of $N_{HL} = 2.6$. Thus, the purely leptonic decay channel does not provide enough statistics to perform a measurement of the ZZZ final states in the near future and other decay modes of the Z boson must be considered in the signature.

The analysis of the $WW\gamma$ final states is performed at the Run 3 centre-of-mass energy of $\sqrt{s} = 13.6$ TeV. The results are compared to an ongoing Run 2 ATLAS analysis with $\mathcal{L}_{int} = 140$ fb^{-1} and a centre-of-mass energy of $\sqrt{s} = 13$ TeV. The signature of the final states consists of the purely leptonic decay channels of the W bosons. To reject contributions from the Z boson decay, the signal is constructed of an OSOF electron-muon pair. Thus, the signature of the $WW\gamma$ final states is: $e^{\pm}\mu^{\mp}\gamma$. The study in this thesis is resulting a signal event expectation of $N = 142 \pm 10$ events, which is 40 % lower than the result in the ATLAS Group analysis. The main background processes, $t\bar{t}\gamma$ and $Z\gamma$, are analysed and the results in the event expectations also differ significantly from the ATLAS analysis.Detailed studies have been performed to understand the observed differences. Potential deviations in

the selection process may exist and lead to differences in the resulting event yields. Further detailed studies are needed in order to investigate both $WW\gamma$ analyses, identify differences and explain the deviations between the event expectations in the $WW\gamma$ signal region.

8 Bibliography

[1] ATLAS Collaboration, *Search for the SM $W^{\pm}W^{\mp}\gamma$ process at the ATLAS detector,* CERN Document Server (Internal Note), ATL-COM-PHYS-2022-163, URL: https://cds.cern.ch/record/2803612

[2] M. Thomson, *Modern Particle Physics,* Cambridge University Press, 2013, ISBN 978-1-107-03426-6.

[3] G. Altarelli, J. Wells, *Gauge Theories and the Standard Model,* Springer International Publishing, pp.1-25, 2017, DOI: 10.1007/978-3-319-51920-3_1.

[4] J. M. Maldacena, *Gravity, particle physics and their unification,* International Journal of Modern Physics A, 15, 2000, DOI: 10.1142/s0217751x00005449, arXiv: hep-ph/0002092.

[5] CERN Homepage, URL: https://home.cern/science/physics/dark-matter, visited 04/29/2024.

[6] S. L. Glashow, *Towards a unified theory: Threads in a tapestry*, Rev. Mod. Phys., 52:3, pp. 539-543, 1980, DOI: 10.1103/RevModPhys.52.539.

[7] A. Salam, *Gauge unification of fundamental forces*, Rev. Mod. Phys., 52:3, pp. 525-538, 1980, DOI: 10.1103/RevModPhys.52.525.

[8] S. Weinberg, *Conceptual foundations of the unified theory of weak and electromagnetic interactions*, Rev. Mod. Phys., 52:3, pp. 515-523, 1980, DOI: 10.1103/RevModPhys.52.515.

[9] N. Cabibbo, *Unitary Symmetry and Leptonic Decays*, Phys. Rev. Lett., 10, pp. 531-533, 1963, DOI: 10.1103/PhysRevLett.10.531.

[10] M. Kobayashi, T. Maskawa, *CP Violation in the Renormalizable Theory of Weak Interaction*, Prog. Theor. Phys., 49, pp. 652-657, 1973, DOI: 10.1143/PTP.49.652.

[11] C. S. Wu *et al.*, *Experimental Test of Parity Conservation in Beta Decay*, Phys. Rev., 105:4, pp. 1413-1414, 1957, DOI: 10.1103/PhysRev.105.1413.

[12] A. Pich, *The Standard Model of Electroweak Interactions*, 2012, arXiv: 1201.0537.

[13] P. Langacker, *Introduction to the Standard Model and Electroweak Physics*, World Scientific, 2010, DOI: 10.1142/9789812838360_0001, arXiv: 0901.0241.

[14] P. Langacker, *Introduction to the Standard Model and Electroweak Physics*, 2010, DOI: 10.1142/9789812838360_0001, arXiv: 0901.0241.

[15] J. Goldstone, *Field Theories with Superconductor Solutions*, Nuovo Cim., 19, pp. 154-164, 1961, DOI: 10.1007/BF02812722.

[16] C. Degrande *et al.*, *Effective field theory: A modern approach to anomalous couplings*, Annals of Physics, 335, pp. 21–32, 2013, DOI: 10.1016/j.aop.2013.04.016, arXiv: 1205.4231.

[17] C. Degrande *et al.*, *Monte Carlo tools for studies of non-standard electroweak gauge boson interactions in multi-boson processes: A Snowmass White Paper*, In Community Summer Study 2013: Snowmass on the Mississippi, 2013, DOI: 10.48550/arXiv.1309.7890, arXiv: 1309.7890.

[18] ATLAS Homepage, URL: https://atlasopendata.docs.cern.ch/docs/documentation/monte_carlo, visited 05/02/2024.

[19] Sherpa Homepage MC simulation, URL: https://sherpa-team.gitlab.io/monte-carlo.html, visited 05/02/2024.

[20] S. Torbjorn, *Monte Carlo Generators*, European School of High-Energy Physics, Aronsborg, Sweden, pp. 51-74, 2006, arXiv: hep-ph/0611247.

[21] S. Agostinelli *et al.*, *Geant4—a simulation toolkit*, Nuclear Instruments and Methods in Physics Research Section A: Accelerators, Spectrometers, Detectors and Associated Equipment, 506:3, pp. 250-303, 2003, DOI: 10.1016/S0168-9002(03)01368-8.

[22] P.J. Clark, *The ATLAS Detector Simulation*, Nuclear Physics B - Proceedings Supplements, 215:1, pp. 85-88, 2011, DOI: 10.1016/j.nuclphysbps.2011.03.142.

[23] ATLAS Collaboration, *Software and computing for Run 3 of the ATLAS experiment at the LHC*, 295, 2024, arXiv: 2404.06335.

[24] R. Brun, F. Rademakers, *ROOT — An object oriented data analysis framework*, Nuclear Instruments and Methods in Physics Research Section A: Accelerators, Spectrometers, Detectors and Associated Equipment, 389:1, pp. 81-86, 1997, DOI: 10.1016/S0168-9002(97)00048-X.

[25] J. Schaarschmidt, *PHYSLITE - A new reduced common data format for ATLAS*, 295, 2024, DOI: 10.1051/epjconf/202429506017.

[26] CERN Homepage, URL: https://www.cern/science/accelerators/high-luminosity-lhc, visited 29/04/2024.

[27] MadGraph Homepage, URL: http://madgraph.phys.ucl.ac.be/, visited 05/02/2024.

[28] S. Torbjorn, S. Mrenna, P. Skands, *A brief introduction to PYTHIA 8.1*, Computer Physics Communications, 178, pp. 852–867, 2008, DOI: 10.1016/j.cpc.2008.01.036, arXiv: 0710.3820v1.

[29] Sherpa Homepage Generator, URL: https://sherpa.hepforge.org/doc/SHERPA-MC-2.2.15.html, visited 05/02/2024.

[30] CERN Homepage, URL: https://home.cern/about, visited 08/06/2024.

[31] L. Evans, P. Bryant, *LHC Machine*, Journal of Instrumentation, 3:08, pp. 81-86, 2008, DOI: 10.1088/1748-0221/3/08/S08001.

[32] ATLAS Homepage, URL: https://atlas.cern/Updates/Briefing/First-Run3-Measurements, visited 15/01/2024.

[33] R. Schmidt, *Accelerator physics and technology of the LHC*, CERN Document Server, 1999, URL: https://cds.cern.ch/record/450636.

[34] CERN Homepage, URL: https://home.cern/news/news/accelerators/spring-awakening-cerns-accelerators-gear-2023, visited 03/01/2024.

[35] ATLAS Homepage, URL: https://home.cern/science/accelerators/accelerator-complex, visited 15/01/2024.

[36] The ATLAS Collaboration, *The ATLAS Experiment at the CERN Large Hadron Collider*, Journal of Instrumentation, 3:08 2008, DOI: 10.1088/1748-0221/3/08/S08003.

[37] The CMS Collaboration, *The CMS experiment at the CERN LHC*, Journal of Instrumentation, 3:08 2008, DOI: 10.1088/1748-0221/3/08/S08004.

[38] ATLAS Homepage, URL: https://home.cern/science/experiments/cms, visited 15/01/2024.

[39] The ALICE Collaboration, *The ALICE experiment at the CERN LHC*, Journal of Instrumentation, 3:08 2008, DOI: 10.1088/1748-0221/3/08/S08002.

[40] The LHCb Collaboration, *The LHCb Detector at the LHC*, Journal of Instrumentation, 3:08 2008, DOI: 10.1088/1748-0221/3/08/S08005.

[41] W. Herr, B. Muratori, *Concept of luminosity*, 2006, DOI: 10.5170/CERN-2006-002.361.

[42] The ATLAS Collaboration, *Expected Performance of the ATLAS Experiment - Detector, Trigger and Physics*, 2009, arXiv: 0901.0512.

[43] G. Aad *et al.*, *The ATLAS Inner Detector commissioning and calibration*, Eur. Phys. J. C, 70, pp. 787-821, 2010, DOI: 10.1140/epjc/s10052-010-1366-7.

[44] The ATLAS Collaboration, *ATLAS muon spectrometer: Technical design report*, CERN Document Server, 1997, URL: https://cds.cern.ch/record/331068.

[45] ATLAS Homepage, URL: https://atlas.cern/Discover/Detector/Calorimeter, visited 19/01/2024.

[46] The ATLAS collaboration, *Operation of the ATLAS trigger system in Run 2*, Journal of Instrumentation, 15:10, 2020, DOI: 10.1088/1748-0221/15/10/P10004.

[47] A. R. Martínez and the ATLAS Collaboration, *The Run-2 ATLAS Trigger System*, Journal of Physics: Conference Series, 762:1, 2016, DOI: 10.1088/1742-6596/762/1/012003.

[48] X. Wu, A. Clark, M. Campanelli, *Electron and photon identification in ATLAS*, Springer Proceedings Physics, 108, 2006, DOI: 10.1007/978-3-540-32841-4_21.

[49] G. Aad *et al.*, *Electron and photon performance measurements with the ATLAS detector using the 2015–2017 LHC proton-proton collision data*, Journal of Instrumentation, 14:12, 2019, DOI: 10.1088/1748-0221/14/12/P12006.

[50] J. Mitrevski, *Electron and Photon Reconstruction with the ATLAS Detector*, Nuclear and Particle Physics Proceedings, pp. 273–275, 2016, DOI: 10.1016/j.nuclphysbps.2015.09.452.

[51] M. Zinser, *Search for New Heavy Charged Bosons and Measurement of High-Mass Drell-Yan Production in Proton—Proton Collisions*, Springer Cham, 2018, DOI: 10.1007/978-3-030-00650-1.

[52] M. Aaboud *et al.*, *Electron reconstruction and identification in the ATLAS experiment using the 2015 and 2016 LHC proton–proton collision data at* $\sqrt{13}$ *TeV*, Eur. Phys. J, 2019, DOI: 10.1140/epjc/s10052-019-7140-6.

[53] L. Marchese, *Lepton and Photon reconstruction and identification performance in ATLAS and CMS*, PoS, 2019, DOI: 10.22323/1.350.0237.

[54] G. Aad *et al.*, *Muon reconstruction performance of the ATLAS detector in proton–proton collision data at* $\sqrt{s} = 13$ *TeV*, Eur. Phys. J., C, 76:5, 2016, DOI: 10.1140/epjc/s10052-016-4120-y, arXiv:1603.05598.

[55] G. Aad *et al.*, *Muon reconstruction and identification efficiency in ATLAS using the full Run 2 pp collision data set at* $\sqrt{s} = 13$ *TeV*, Eur. Phys. J., C, 81, 2021, DOI: 10.1140/epjc/s10052-021-09233-2.

[56] ATLAS Collaboration, *Performance of missing transverse momentum reconstruction for the ATLAS detector in the first proton-proton collisions at* $\sqrt{s}$= *13 TeV*, 2015, URL: https://cds.cern.ch/record/2037904?ln=de.

[57] PDG Homepage, URL: https://pdg.lbl.gov/2023/tables/contents_tables.html, visited 05/03/2024.

[58] M. Aaboud, *et al.*, $ZZ \rightarrow l^+l^-l'^+l'^-$ *cross-section measurements and search for anomalous triple gauge couplings in 13 TeV in pp collisions with the ATLAS detector*, Physical Review D, 97:03, 2018, DOI:10.1103/physrevd.97.032005.

[59] G. Aad *et al.*, *ATLAS data quality operations and performance for 2015–2018 data-taking*, Journal of Instrumentation, 15:04, 2020, DOI: 10.1088/1748-0221/15/04/P04003.

[60] G. Aad *et al.*, *Electron and photon efficiencies in LHC Run 2 with the ATLAS experiment*, Journal of High Energy Physics, 2024, DOI: 10.1007/jhep05(2024)162.

[61] G. Aad *et al.*, *Muon reconstruction and identification efficiency in ATLAS using the full Run 2 pp collision data set at* $\sqrt{s} = 13$ *TeV*, The European Physical Journal C, 2020, DOI: 10.1140/epjc/s10052-021-09233-2.

[62] ATLAS Collaboration, *ATLAS detector and physics performance: Technical Design Report*, CERN Dokument Server, 1, 1999, URL: https://cds.cern.ch/record/391176.

[63] G. Aad *et al.*, *Electron and photon performance measurements with the ATLAS detector using the 2015–2017 LHC proton-proton collision data*, Journal of Instrumentation, 14:12, 2019, DOI: 10.1088/1748-0221/14/12/p12006.

[64] M. Aaboud *et al.*, *Measurement of fiducial and differential* W^+W^- *production cross-sections at* $\sqrt{s} = 13$ *TeV with the ATLAS detector*, Eur. Phys. J. C, 79:10, 2019, DOI: 10.1140/epjc/s10052-019-7371-6.

[65] P. A. Zyla *et al.*, *Review of Particle Physics*, Progress of Theoretical and Experimental Physics, 2020, DOI:10.1093/ptep/ptaa104.

[66] PDG Homepage, URL: https://pdg.lbl.gov/2019/tables/rpp2019-sum-quarks.pdf, visited 13/04/2024.

[67] P. Ott, *Measurement of* $Z\gamma\gamma$ *production in pp collisions at* $\sqrt{s} = 13$ TeV *with the ATLAS detector*, Universität Heidelberg, 2023, URL: https://www.kip.uni-heidelberg.de/Veroeffentlichungen/details.php?id=4601#start.

[68] A. Ackermann, *Measurement of the* $ZZ\gamma$ *final state with the ATLAS detector at the LHC*, Universität Heidelberg, 2022, URL: https://www.kip.uni-heidelberg.de/Veroeffentlichungen/details.php?id=4537#start.

[69] O. Brüning, *et al.*, *The scientific potential and technological challenges of the High-Luminosity Large Hadron Collider program*, Reports on Progress in Physics, 85:4, 2022, DOI:10.1088/1361-6633/ac5106.

[70] M. Aaboud, *et al.*, *Study of $WW\gamma$ and $WZ\gamma$ production in pp collisions at $\sqrt{s} = 8$ TeV and search for anomalous quartic gauge couplings with the ATLAS experiment*, Eur. Phys. J. C, 77, 2017, DOI:10.1140/epjc/s10052-017-5180-3.

[71] PDG Homepage, URL: https://pdg.lbl.gov/2019/listings/rpp2019-list-w-boson.pdf, visited 20/05/2024.

[72] M. Aaboud *et al.*, *Measurement of the photon identification efficiencies with the ATLAS detector using LHC Run 2 data collected in 2015 and 2016*, Eur. Phys. J. C, 79:205, 2019, DOI: 10.1140/epjc/s10052-019-6650-6.

[73] F. Giuli, *Performance of Monte Carlo Event Generators for the Production of Boson and Multi-Boson States ATLAS Analysis*, High Energy Physics, 2017, arXiv: 1709.00492.

[74] ATLAS Collaboration, *ATLAS simulation of boson plus jets processes in Run 2*, Cern Document Server, 2017, URL: https://cds.cern.ch/record/2261937.

Erklärung:

Ich versichere, dass ich diese Arbeit selbstständig verfasst und keine anderen als die angegebenen Quellen und Hilfsmittel benutzt habe.

Heidelberg, den 19.06.2024